Department of Physics and Astronomy
University of Heidelberg

Bachelor Thesis in Physics
submitted by

Sven Hoppner

born in Heidelberg (Germany)

2020

Implementation of a Stand Alone Tracking Algorithm for the Transition Radiation Detector in ALICE using a Kalman Filter Approach

This Bachelor Thesis has been carried out by Sven Hoppner at the
Physikalisches Institut in Heidelberg
under the supervision of
Priv. Doz. Dr. Yvonne Pachmayer

Abstract

Within the scope of this bachelor thesis a stand alone tracking algorithm for the Transition Radiation Detector (TRD) in ALICE was implemented using a Kalman filter approach. For testing and benchmarking purposes a simple Monte Carlo simulation of the TRD was developed. Different algorithms, including a straight line tracking algorithm and two Kalman filters with realistic track models were tested and their efficiencies and purities compared. Based on the experience of the Monte Carlo simulation, a Kalman filter based stand alone tracking algorithm was developed and applied to real p–Pb data recorded at $\sqrt{s_{\mathrm{NN}}} = 5.02\,\mathrm{TeV}$. The track reconstruction efficiency and transverse momentum resolution was determined using tracks from the Time Projection Chamber (TPC) in ALICE which were matched to Kalman filter tracks. The stand alone tracking algorithm was further used to identify and study photon conversions in front of and within the TRD. Furthermore, nuclear interactions which happened in front of and within the TRD were successfully reconstructed by identifying the resulting particle shower.

Zusammenfassung

Im Rahmen dieser Bachelorarbeit wurde ein unabhängiger Tracking-Algorithmus für den Transistion Radiation Detector (TRD) von ALICE unter Verwendung eines Kalman-Filter-Ansatzes implementiert. Zu Test- und Benchmarkingzwecken wurde eine einfache Monte Carlo Simulation des TRDs erstellt. Verschiedene Algorithmen, darunter ein einfacher Tracking-Algorithmus und zwei Kalman-Filter mit realistischen Track-Modellen wurden getestet und ihre Spurrekonstruktionseffizienz und Reinheit verglichen. Basierend auf den Erfahrungen mit der Monte Carlo Simulation wurde ein eigenständiger Tracking-Algorithmus basierend auf einem Kalman Filter entwickelt und auf p–Pb-Daten mit $\sqrt{s_{\mathrm{NN}}} = 5.02\,\mathrm{TeV}$ angewendet. Die Spurrekonstruktionseffizienz und die transversale Impulsauflösung wurden unter Verwendung von Spuren aus der Time Projection Chamber in ALICE, welche zu Kalman Spuren zugeordnet wurden, bestimmt. Der unabhängige Tracking-Algorithmus wurde des Weiteren verwendet, um Photonenkonversionen vor und innerhalb des TRD zu identifizieren und zu untersuchen. Darüber hinaus wurden nukleare Wechselwirkungen, die vor und innerhalb des TRD auftraten, erfolgreich rekonstruiert, indem die resultierenden Teilchen identifiziert wurden.

Contents

List of Figures

List of Tables

1 Introduction

The quark-gluon plasma (QGP) is a state of matter, which is believed to have been present shortly after the Big Bang [1]. The QGP has a very high temperature, a high energy density and the quarks and gluons are in a deconfined state [2]. Deconfinement describes a state in which quarks (the elementary particles which make up hadrons like protons or neutrons) are no longer bound to each other by their strong interaction. Deconfinement only happens when the nuclear matter experiences extreme temperatures and/or high pressure. The task of studying the quark-gluon plasma phase was taken up by the researchers at CERN (Conseil Européen pour la Recherche Nucléaire, European Organisation for Nuclear Research). The Large Hadron Collider (LHC) is located at CERN, where it is possible to generate this state of matter by colliding heavy nuclei at relativistic energies. Other places with suitable hadron colliders include the Relativistic Heavy Ion Collider (RHIC) in New York. The LHC is the largest, most powerful particle collider of the world (as of 2020). Alongside the LHC are other particle accelerators at CERN from older experiments like the Proton Synchrotron (PS) or the Super Proton Synchrotron (SPS) which led to first evidence of the quark-gluon plasma [3–6]. At the LHC are currently four major detectors in operation: ATLAS (**A** **T**oroidal **L**HC **A**pparatu**S**), the largest detector of the four, CMS (**C**ompact **M**uon **S**olenoid), LHCb (**L**arge **H**adron **C**ollider **b**eauty) and the ALICE (**A** **L**arge **I**on **C**ollider **E**xperiment) detector. A schematic view of the LHC and its major experiments at CERN can be seen in Fig. 1.1. Those four detectors are used to study different fields of particle and heavy–ion physics with the ALICE detector specifically build to study the QGP. The LHC is currently in the Long Shutdown 2 in which the detectors (including ALICE) are repaired and upgraded for the upcoming Run 3 of the LHC. ALICE is suited for studying the QGP because of its excellent tracking performance even in high-multiplicity environments and particle identification (PID) capabilities for a large range of momenta. ALICE records high energy proton–proton collisions for energies up to 13 TeV and lead–lead collisions with energies up to 5.02 TeV/nucleon. The ALICE experiment achieves its excellent tracking performance with a range of individual detector systems, one of them being the Transition Radiation Detector (TRD). The TRD is mainly used for particle identification and triggering of electrons, jets and light nuclei. The scope of this work is to improve the tracking capabilities of the ALICE detector by implementing a stand-alone tracking using a Kalman filter approach for the TRD. A stand-alone tracking algorithm in the TRD would be beneficial by tracking nuclear interactions of traversing particles as well as photon conversions within the TRD. Since photons do not interact strongly, they can grant access to information on the early phases of heavy–ion collisions. This includes the temperature of the initial QGP and the elliptic flow [7]. The reconstruction of nuclear interaction allows nuclear interaction cross sections for rare atoms like $\overline{^3\mathrm{He}}$ to be measured. Also a atand-alone tracking grants the possibility of finding late decays which happen after the main tracking detectors and the independent tracking

algorithm can be used for additional secondary vertex finding and to improve the tracking overall. The TRD has many properties which make it ideal for reconstructing photon conversions and nuclear interactions: The TRD has a high material budget compared to similar detectors which increases the interaction propability for photon conversions and nuclear interactions, the TRD is a faster detector than the TPC which results in a lower pile-up and also low p_T photon conversions can be reconstructed in the TRD whereas the efficiency of the TPC is low for low p_T particles. In addition the reconstruction algorithm within this thesis is a new development which grants the full control to make it perfectly suitable for the physics studies one wants to research and one does not have to rely on previously existing tracking algorithms. A TRD stand-alone tracking can also be used to calibrate the TRD drift velocity for the upcoming run of the LHC. This work is structured in five chapters: In chapter 1 a short introduction to the ALICE detector and the theoretical foundations of the Kalman filter is given. In chapter 2 the Monte Carlo (MC) simulation of the TRD and the tracking algorithms implemented for the MC simulation are described. In chapter 3 the Kalman filter tracking algorithm implemented for real data and the performance measurements are explained. In chapter 4 the physical results aquired with the Kalman filter are described and in chapter 5 a conclusion of the thesis and an outlook on further improvements is given.

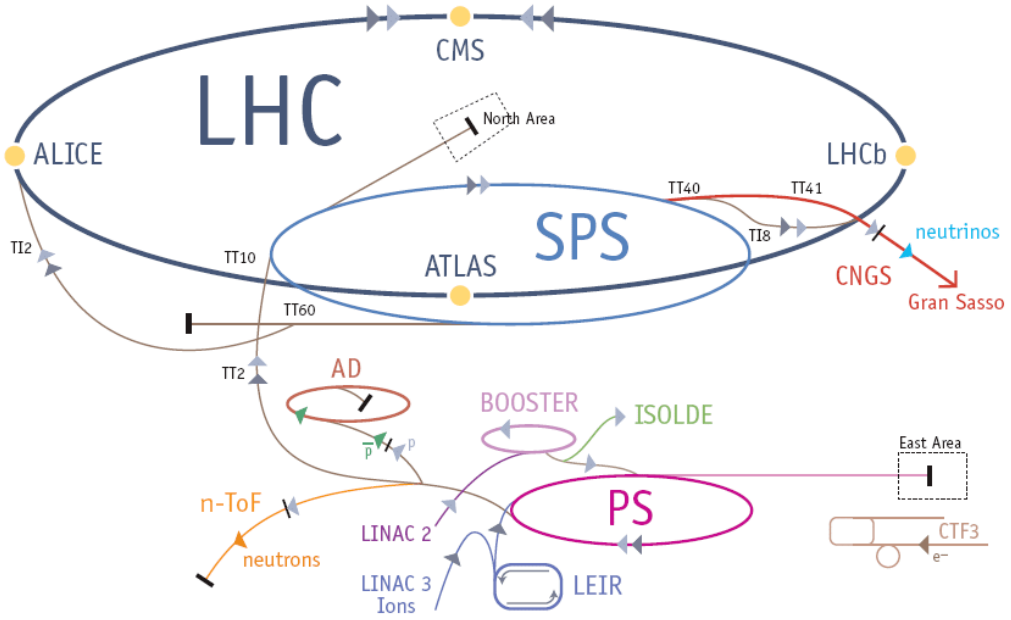

Figure 1.1: Schematic drawing of the different particle accelerators and facilities at CERN. The drawing is taken from [8].

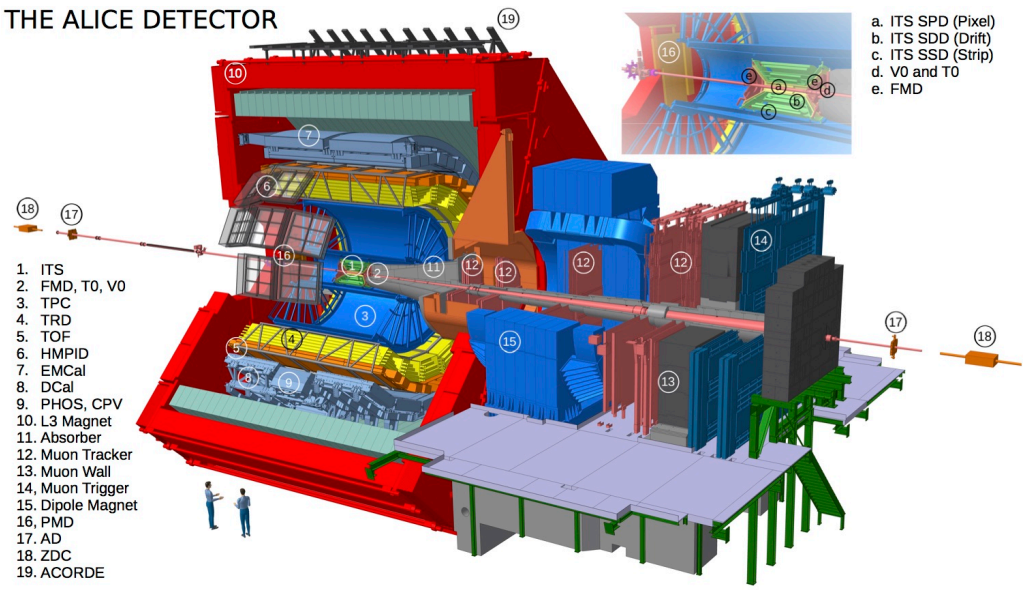

Figure 1.2: Schematic drawing of the ALICE detector. The central barrel (numbers 1–10) as well as the muon arm (numbers 11–15) are shown. The central barrel contains e.g. the Inner Tracking System (ITS), Time Projection Chamer (TPC) and Transition Radiation Detector (TRD) which were indispensable for this work as well as a Time-Of-Flight Detector (TOF), several calorimeters and the 0.5 T solenoid. Drawing taken from [9].

1.1 The ALICE Detector

In this section the ALICE detector setup will be explained in more detail. ALICE (**A** **L**arge **I**on **C**ollider **E**xperiment) is a general-purpose detector which was built for heavy-ion experiments at the LHC and optimized for particle identification and tracking even in high–particle density environments of around 8000 charged particles per pseudorapidity [10]. The studied collisions with ALICE are lead–lead, proton–lead and proton–proton collisions. At the standard magentic field strenght of B = 0.5 T a minimum p_T of around 200 MeV/c is needed for tracks to reach the outer radius of the TPC. Lower p_T tracks start curling within the active TPC volume but can still be reconstructed down to a few 100 MeV/c [11]. ALICE is capable of performing particle identification of charged particles with a momentum well over 100 GeV/c [11]. A schematic view of the ALICE detector can be seen in Fig. 1.2. The setup is not symmetrical along the beamline, so the right side in figure 1.2 is called the C–side (C stands for clockwise which is related to the direction of the beam in the LHC) and the left side is called the A–side (anti–clockwise). The detector occupies a space of $16 \times 16 \times 26\,\mathrm{m}^3$ and weighs about 10 000 t. The detector itself consists of a setup with several layers of multiple subdetectors, each with a specific purpose assigned to them. From inside out as can be seen in Fig. 1.2 there is the inner tracking

system (ITS) which is enclosed by the Time Projection Chamber (TPC) and the Transition Radiation Detector (TRD). Around the TRD is the Time-Of-Flight detector (TOF). Then there are the different calorimeters: the Electromagnetic Calorimeter (EMCAL), the Di-jet Calorimeter (DCAL), the Photon Spectrometer (PHOS) and a Cherenkov detektor (HMPID, which is an acronym for High Momentum Particle Identification). The detectors are enclosed in a large solenoid which provides the ALICE detector with a magnetic field of up to 0.5 T, which is directed along the z-axis. The solenoid marks the end of the central barrel. In addition there are detectors for particle multiplicity measurements and on the C-side are more detectors which are used for muon detection. This C-side part of the detector is called the muon arm and it is not relevant for the implementation of the Kalman filter. In the following sections the TRD, from which the data the Kalman Tracking algorithm was implemented for is coming from, as well as the ITS and the TPC detector, from which the data for the current tracking is coming from and which was used to measure the accuracy of the algorithm, will be explained further.

1.1.1 Inner Tracking System

The Inner Tracking System (ITS) consists of three different types of silicon semiconductor detectors as can be seen in the inlet of Fig. 1.2. The first is a silicon pixel detector followed by a silicon drift detector and then a silicon strip detector. In the ITS two successive layers of each silicon detector is build in, to get a total of six silicon detector layers. The ITS covers a pseudorapidity range of $|\eta| < 0.9$ and it covers the radii between 39 and 430 mm. Since the ITS is the detector closest to the interaction point it plays a crucial role in nearly all measurements performed in the central barrel of the ALICE detector. It is used to reconstruct the primary vertex with a high resolution, to identify and track particles with too small energies to reach the TPC. For tracks which are reconstructed with the TPC it is used to improve the momentum and pointing resolution. It is also build in a way which minimizes the impact on the particle trajectory by having a small material budget. A physics purpose of the ITS is to identify D-meson decays which have a decay length of below 100 µm. For LHC Run 3 the ITS will be replaced by a new detector[12].

1.1.2 Time Projection Chamber

The Time Projection Chamber (TPC) is the main device for tracking and particle identification in ALICE. It has a radial active coverage from 0.83 to 2.50 m and equally to the ITS it covers a pseudorapidity range of $|\eta| < 0.9$. It can fully reconstruct charged particles with a transverse momentum of $p_T \geqslant 100\,\mathrm{MeV}/c$. The TPC consists of a barrel filled with a mixture of argon and CO_2 gas. Charged particles ionize the gas along their

trajectory. The TPC consists of 159 pad rows at each end in radial direction which are used to measure the x–y position of the incoming drifting electrons from the ionization process. In addition it measures the drift time to reconstruct together with the known drift velocity the z–position of each ionization cluster. The amount of deposited charge can also be measured which can then be used to identify the traversing particles in a wide range of momentum. For this the deposited energy per unit of length is fitted after truncation with a Bethe function which gives a hypothesis for the true particle species.

1.1.3 Transition Radiation Detector

The Transition Radiation Detector (TRD) is used to provide triggering capabilities of high momentum electrons, jets and light nuclei and particle identification of electrons with a transverse momentum of $p_T \geqslant 1\,\mathrm{GeV}/c$ [13]. The TRD consist of 522 individual readout detector modules as depicted in figure 1.3. The readout modules are placed in 18 supermodules, each consisting of 5 stacks along the beamline direction, and 6 layers arranged in radial direction (see Fig. 1.3). The TRD covers a pseudorapidity range of $|\eta| < 0.84$ and the active radius is from 2.90 to 3.68 m. The different detector elements have an area from $0.90\times\ 1.06\,\mathrm{m}^2$ up to $1.13\times\ 1.43\,\mathrm{m}^2$ [13]. Each detector element (see Fig. 1.4) consists of a sandwich radiator with a thickness of 48 mm, a drift section of 30 mm which is filled with a Xe-CO_2 mixture and a multi-wire proportional chamber (MWPC) section with pad readout (7 mm). The readout pads are supported by a honeycomb sandwich back panel made of carbon fiber (22 mm) to withstand overpressures of up to 1 mbar. The electronics mounted on top of the detector is water cooled which increases the thickness of a single detector layer to a total of 125 mm per detector layer and a total radiation length of $X/X_0 = 2.85\,\%$ [13]. The TRD pad planes consist of 144 columns and 12 – 16 rows depending on the size of the chamber.

1.1.3.1 Tracklet Reconstruction & Calibration

In Fig. 1.4 a schematic cross section of a TRD chamber is shown as well as the response to traversing particles. Charged particles first pass the radiator where electrons with a Lorentz factor $\gamma > 800$ produce transition radiation (TR) photons which are then absorbed by the detector gas in the drift region (depicted as a larger red dot). This allows one to differentiate between electrons and other charged particles like pions. The traversing particles ionize the Xe-CO_2 mixture which produces ionisation electrons and ions. The electrons then travel through the drift region to the anode wires because of the applied electric field. Because of the B–field a sideway force is applied to the electrons so they do not drift directly along the field lines of the electrostatic field but in an angle to the field lines called the Lorentz angle which is an effect that has to be corrected for during

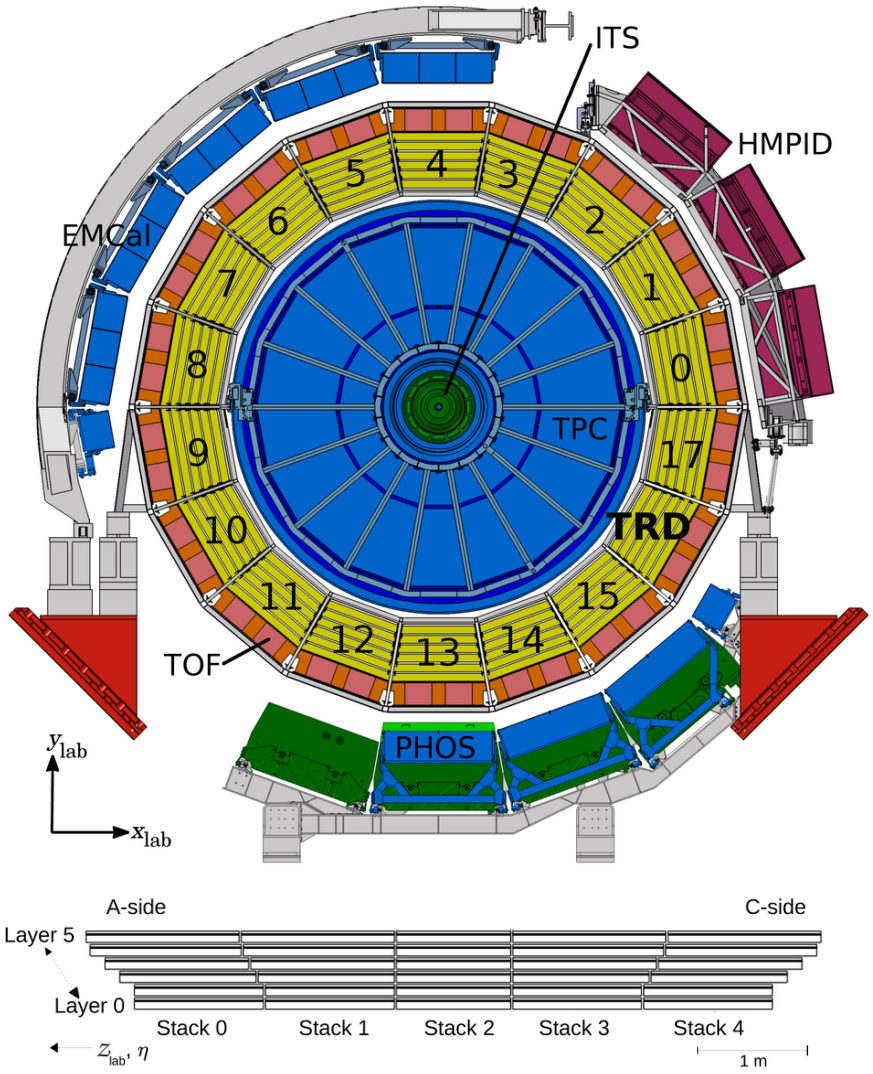

Figure 1.3: Schematic drawing of the cross section of the ALICE detector (top) and the side view of one TRD supermodule (bottom). Figure taken from [13].

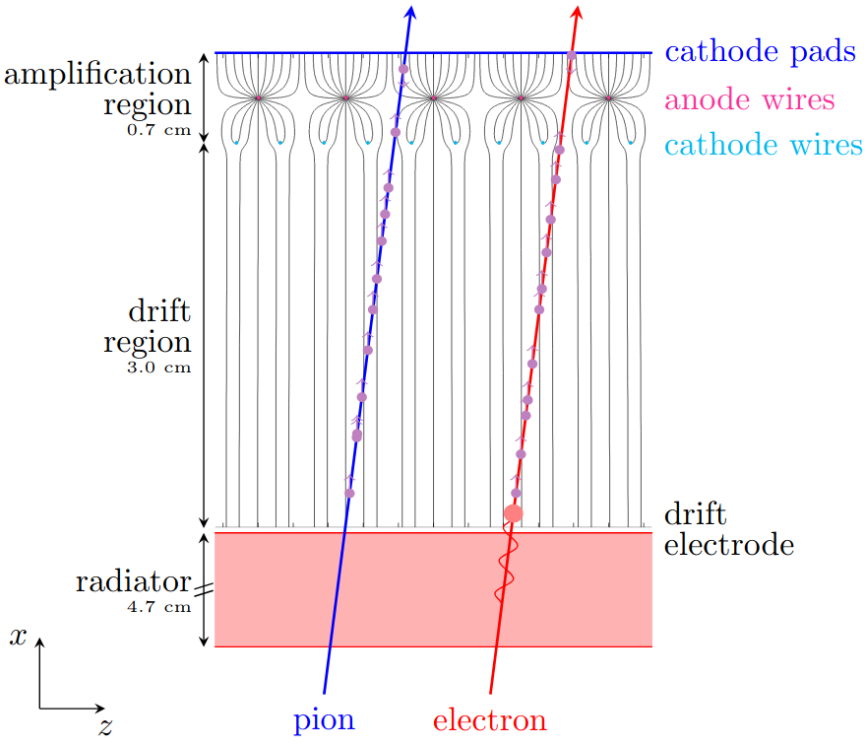

Figure 1.4: Schematic cross section of a TRD chamber in the local x-z plane. To illustrate the ionization and transition radiation contribution two particle tracks are depicted. The electron traverses through the radiator creating transition radiation which is absorbed by the detector gas (depicted by a red dot). Figure taken from [13]

the calibration and reconstruction procedure. The ionized electrons travel along the drift lines (depicted by the black lines in Fig. 1.4) and are accelerated for short distances on their way to the anode. On their way they collide with particles in the detector gas which slows the ionized electrons down and results in a constant drift velocity. Close to the anode wires they ionize the detector gas and the created electrons then again drift to the anode and create more ions and electrons on their way. The number of ions produced increaces exponentially the closer the electrons are to the anode. The effect that a single produced electron is able to ionize many atoms is called the avalanche effect and and for the TRD a gas amplification of around 3000 is achieved. The produced ions then travel to the cathode pads where they induce a signal which is measured. Because the electrons drift to the anode wires which takes more time the longer the distance is, the last electron produced by the primary particle gets detected first, while the first electron produced by the primary particle gets detected last. The raw data of these measurements consists of the position and ADC values of the hit readout pads for each of 24 time bins per measurement. To reconstruct the path of a passing particle in one chamber (called a tracklet), a linear fit is made to the mean positions of hit pads of all time bins. For the

tracklet reconstruction the measured drift time per pad needs to be converted into a drift length using a calibrated drift velocity. In this calculation the ion tail effect needs to be considered which is correlating the measured ADC values between several time bins due to the slow drift of the ions. A new drift velocity calibration procedure is correcting this effect [14]. The resulting data consists of one offset vector and one direction vector for each measurement and one measurement marks one tracklet. The uncertainty of the offset measurement is in the order of 1.1 to 1.2 mm and the uncertainty of the direction vector is in the order of 3.5° [15]. The information of the measured tracklets is used within this thesis.

1.2 The Kalman filter

1.2.1 Theoretical Foundation

The Kalman filter is an algorithm for stochastic estimation of a current state in a system from noisy measurements and finds use in numerous technological applications such as navigation and control of vehicles like space- or aircraft as well as trajectory optimization and particle tracking and many more [16–18]. The Kalman filter is named after Rudolf E. Kálmán who described the algorithm around 1960 [19]. It consists of two repetitive successive processes with the first being the prediction step and the second the correction step. During the prediction step the Kalman filter calculates an estimate of the current state vector based on the last state vector $s_{k|k-1}$ at a given time t_k along with its uncertainties depicted in a covariance matrix $\mathbf{P}_{k|k-1}$. The index k represents the iteration of the Kalman filter where one iteration marks one prediction step and one correction step. Because of the TRD detector geometry a local coordinate system is used for the parameterization of the particle tracks, which is explained further in section 1.2.2. The local coordinate system allows for the local x-coordinate x_k to be used as propagation variable instead of the time. In the correction step the current estimate is updated to the new state vector s_k based on a made measurement m_k of the state vector along with its measurement uncertainty δ_k. After the correction the algorithm starts again from the prediction with the new state vector. A scheme of this iterative algorithm along with the used formulas can be seen in Fig. 1.6. The Kalman filter model presupposes that the state at time t_k is a linear transformation of the state at the plane x_{k-1} along with a Gaussian distributed propagation uncertainty ϵ_k and that the measurement is a linear representation of the current state vector:

$$s_k = f_k(s_{k-1}) + \epsilon_k, \tag{1.1}$$

$$m_k = \mathbf{C}s_k \quad + \delta_k, \tag{1.2}$$

with f_k representing the known propagation function explained further in chapter 1.2.4 and $\mathbf{C}$ is the observation model which transforms the state space into the observation space vector. The Kalman filter is based on the assumption that the uncertainties in the measurement as well as the state vector uncertainties follow a Gaussian distribution with a mean of zero.
In Fig. 1.5 the working principle of the Kalman filter is depicted. The figure shows the six layers of the TRD with a particle traversing these and which results in the measurements consisting of an offset and a direction vector for each layer. As shown the algorithm starts with a seed consisting of an initial guess for the state vector and the track covariance matrix at the outermost layer. One reason for starting at the last layer is because of the spread of the particle tracks. The detector chambers which are further away from the collision experience a lower occupancy of primary tracks since the tracks are distributed over a larger surface area. The closer chambers to the primary vertex have larger amounts of low energy electrons which increases the noise and makes it harder to do a proper seeding and tracking. Another reason for starting at the last layer of the TRD is that particles which split up while they are within the TRD, i.e. photons which split up in a positron and an electron, are hard to track while going from the inner to the outer layers. This is the case because the split has to be recognized which requires further selection criterias, and the two different tracks have to be tracked individually, but operating the Kalman tracking algorithm in reverse eliminates this problem since the split up tracks are seperate from the start and can be merged easily after the tracking. The acquisition of the seed is described in section 1.2.3. In Fig. 1.5 the seed consists of one starting tracklet from which the first prediction is calculated. During the prediction phase the state vector and the corresponding covariance matrix are given by

$$s_{k|k-1} = f_k(s_{k-1}), \text{ and} \tag{1.3}$$

$$\mathbf{P}_{k|k-1} = \mathbf{F}_k \mathbf{P}_{k-1} \mathbf{F}_k^T + \mathbf{Q}_k, \tag{1.4}$$

$$\text{with } \mathbf{F}_k = \frac{\partial f_k}{\partial s_{k-1}}. \tag{1.5}$$

$\mathbf{F}_k$ is a Jacobian matrix with entries calculated from the derivatives of the propagation function of the state vector entries (see section 1.2.4) and $\mathbf{Q}_k$ is the prediction uncertainty covariance matrix. The predicted position and direction of the state vector at the next lower layer is depicted in green in Fig. 1.5. The next step is the search for a fitting tracklet for the track to be used as next measurement. If the next tracklet in the track is not already known, which would be the case if the next measurement is given by the seed (see 1.2.3), a χ^2 selection criterion is used to select a fitting tracklet. To accept or reject TRD tracklets as new measurements for the path the predicted χ^2-increment is calculated

by

$$\chi^2_{k|k-1} = (r_{k|k-1})^T (\mathbf{R}_{k|k-1})^{-1} (r_{k|k-1}), \tag{1.6}$$

$$\text{with } r_{k|k-1} = m_k - \mathbf{C} s_{k|k-1}, \tag{1.7}$$

$$\text{and } \mathbf{R}_{k|k-1} = \mathbf{V} + \mathbf{C}\mathbf{P}_{k|k-1}\mathbf{C}^T. \tag{1.8}$$

Here $\mathbf{V}$ is the covariance matrix of the measurement. Should the predicted χ^2-increment of a tracklet be lower than a certain threshold and also lower than the χ^2-increment of every other tracklet then it gets selected as the next measurement in the tracks path. After a tracklet is selected the corrected estimate and track covariance matrix is calculated with

$$s_k = s_{k|k-1} + \mathbf{K}_k (m_k - \mathbf{C} s_{k|k-1}), \text{ and} \tag{1.9}$$

$$\mathbf{P}_k = \mathbf{P}_{k|k-1} (\mathbb{1} - \mathbf{K}_k \mathbf{C}), \tag{1.10}$$

$$\text{with } \mathbf{K}_k = \mathbf{P}_{k|k-1}\mathbf{C}(\mathbf{V} + \mathbf{C}\mathbf{P}_{k|k-1}\mathbf{C}^T)^{-1}. \tag{1.11}$$

$\mathbf{K}_k$ represents the Kalman gain matrix which is used to minimize the residual uncertainty. In Fig. 1.5 the corrected state vectors are depicted as red arrows. After the optimal estimate got calculated the χ^2-increment at the new estimate is determined by

$$\chi^2_k = (r_k)^T (\mathbf{R}_k)^{-1} (r_k), \tag{1.12}$$

$$\text{with } r_k = m_k - \mathbf{C} s_k, \tag{1.13}$$

$$\text{and } \mathbf{R}_k = \mathbf{V} + \mathbf{C}\mathbf{P}_k\mathbf{C}^T. \tag{1.14}$$

1.2.2 Local Coordinate System of the TRD

The TRD data consists of every tracklet measured in the event and for each tracklet the offset position and the direction vector is saved in global coordinates additionally to the detector chamber in which it was detected. The global coordinate system has its origin at the center of the TRD. It is a right-handed cartesian coordinate system with the z–axis along the beam axis, the x–axis pointing at the gap between supermodules 17 and 0 and the y–axis pointing at the center of supermodule 4. The measured tracklets only have their location and direction saved but not their momentum or the time of detection. Theoretically the time of detection would have been used in the Kalman filter to calculate the estimated position at a given time and then search at the propagated position for new tracklets to assign to the track but instead the radial distance to the interaction point is used as an equivalent to the time, since the information about the time of detection is

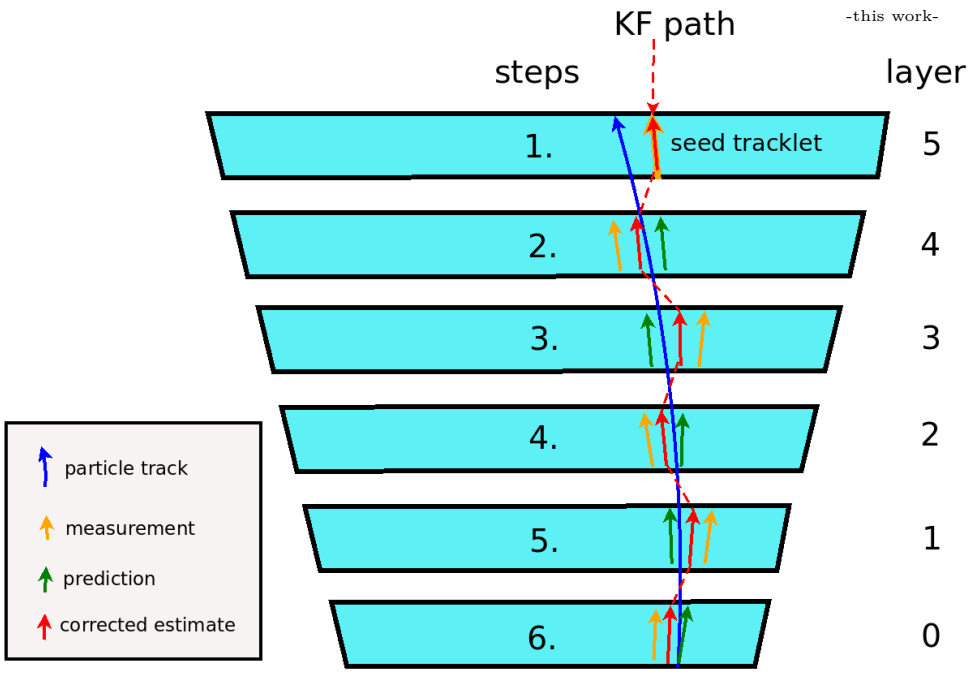

Figure 1.5: Schematic drawing of the Kalman filter in use. The particle track (depicted in blue) represents the real track of the passing particle. The measurements corresponding to the particle track are shown in orange. The Kalman filter algorithm starts at the outermost layer going inwards with a seed from which position and direction of the first prediction of the new state vector is calculated (green arrows). On the basis of the predicted state vector the next measurement is selected and with this the corrected estimates are calculated (shown as red arrows). The uncertainties of the measurements are exaggerated.

not given by the detector. The current position of a particle along with its orientation in dependency of the radial distance to the interaction point is called the state vector. The state vector has to have all variables which are needed to fully describe the particle track with exception to the propagation constant (the radial distance) which is stored separately. In this case the state vector consists of six variables: three entries are needed to describe the current position, two for the direction and one used to describe the curvature since the particles trajectories follow a helical path through the detector based on their momentum and their charge. To reduce the computational complexity of the Kalman propagation, it is advised to have a state vector with as less variables as possible. Since the x and y coordinates are connected to each other by the current radius of the particle, one of them can be omitted. To do this the Kalman filter is not using the global coordinate system but instead uses a local coordinate system for each supermodule. For this the global coordinate system and all tracklet positions and directions of the supermodule are rotated along the z-axis such that the x-axis always points to the center of the supermodule and represents the radial distance. The local coordinate system can be seen in Fig. 1.7. Now the state

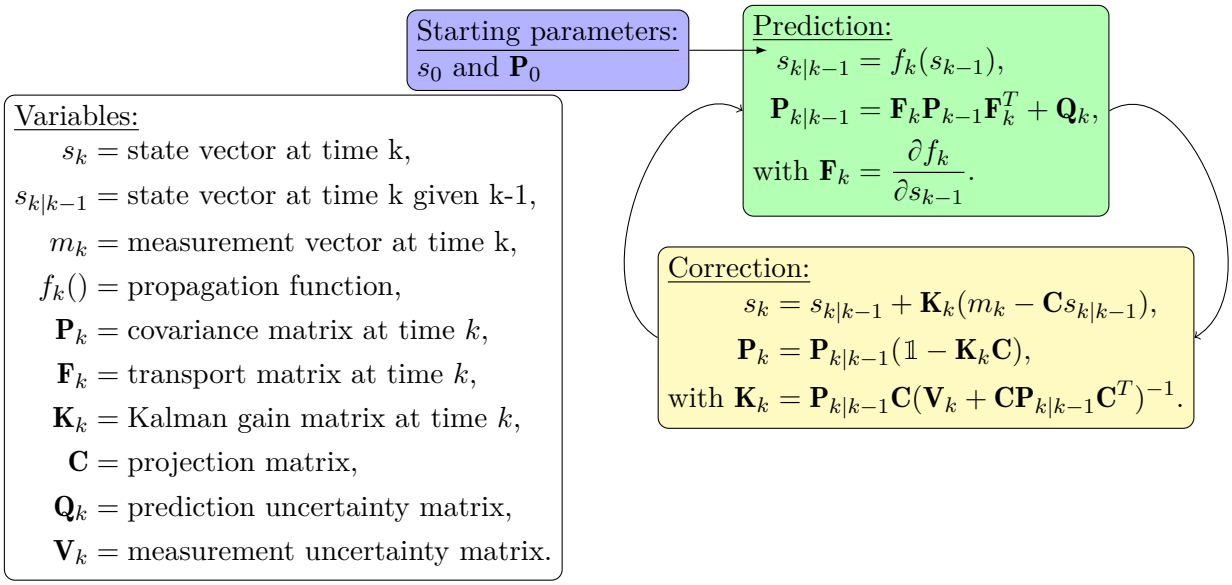

Figure 1.6: Scheme of the Kalman filter iterative algorithm.

vector can be expressed by only five variables:

$$s = (y, z, \sin\phi, \tan\lambda, q/p_T)^T, \tag{1.15}$$

where y and z describe the offset position, ϕ describes the azimuthal angle, λ describes the polar angle and q/p_T describes the charge divided by the transverse momentum of the particle which gives information about the curvature of the particle track. After completion of the track reconstruction, the helix parameters are returned in the global coordinate system.

1.2.3 Seeding

As mentioned in section 1.2.1 a tracking algorithm using the Kalman filter technique requires a starting point which can not be acquired by the Kalman filter itself. This starting point is called the ”seed” and its acquisition is described in the following. The purpose of the seeding algorithm is to find two tracklets which fulfill a series of requirements to be considered for a possible track. For the seeding a straight line track is assumed and one tracklet has to fit to another tracklet within two layers below it. Every tracklet of every layer which has not already been associated with a track gets checked whether in the two detectors below it is one tracklet that satisfies the criteria on position and direction. For that the directions of the tracklets, as well as the positions of both have to match within a defined range. A search through multiple layers is necessary for the seeding algorithm to increase the possibility of finding a seed despite of missing tracklets and turned off TRD

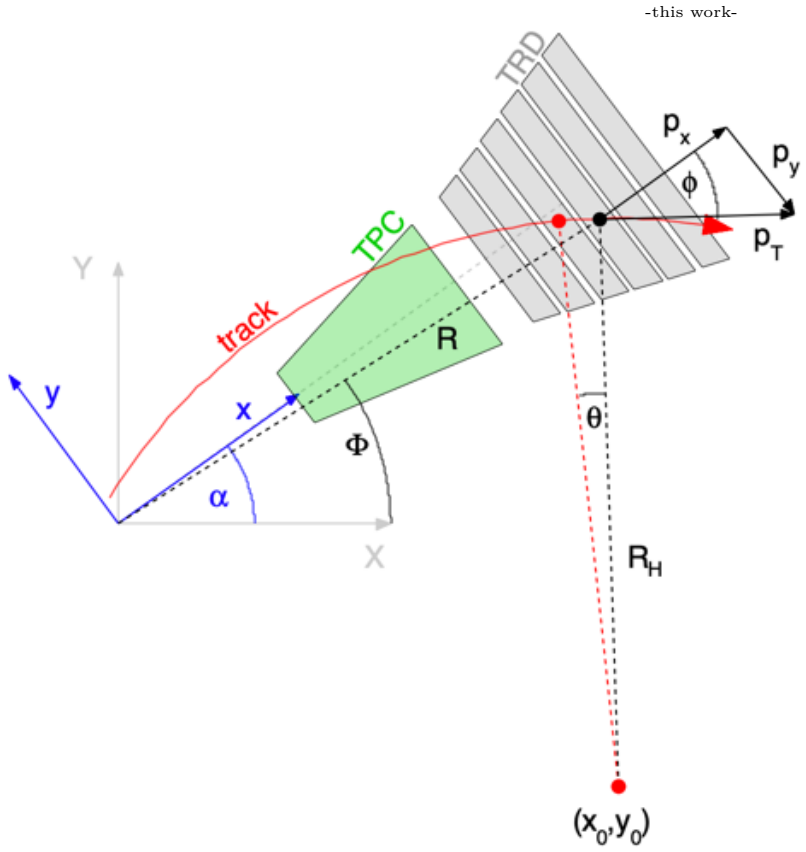

Figure 1.7: Schematic view of a particle passing though the detector together with the definition of important variables used for the TRD Kalman tracking. The global coordinate system (X,Y,Z) is rotated into the local coordinate system (x,y,z) by the angle α. The particle is propagated from one layer of the TRD to the next with a given step length.

chambers (layers). To match two individual tracklets for the Kalman filter on real data, the angle between their direction vectors has to be below 15°, the distance in y direction has to be below 7 cm and in z direction below 20 cm. The difference in x direction is always 0 cm since the outer tracklet gets propagated linearly to the right x plane. The range for a matching pair is set as large as possible to cope with the measurement uncertainties and the linear propagation. The parameters of the seeding algorithm were selected by arbitrarily setting the values and iteratively increasing the uncertainties until a correct seed was found for almost all tracks from the TPC detector. The parameters are set in this way to achieve a high efficiency of the Kalman filter with fewer regards to purity. The outer tracklet gets defined as the seed for the Kalman filter and the inner tracklet is the first measurement for the correction phase of the Kalman filter. The principle is described in more detail in section 2.1.

1.2.4 Track Model

As described in section 1.2.1 a propagation function is needed to get from one state vector to the next (see Equation (1.1)). The use of a local coordinate system (see chapter 1.2.3) allows the x-coordinate as propagation variable and a 5D state vector to be used (see Equation (1.15)). The five variables of the state vector along with the information about the current propagation variable x_k is enough to completely describe the helical path of the particles in the ALICE detector. For each of these state variables the new position needs to be calculated, for which the difference to the new position Δs is added to the last position:

$$s_{k+1} = s_k + \Delta s. \tag{1.16}$$

The different entries of Δs need to be calculated individually and are given by the following equations which were taken from [20]:

$$\Delta y = y_{k+1} - y_k = R_H \left(\sqrt{1 - \sin(\phi_k)^2} - \sqrt{1 - \sin(\phi_{k+1})^2} \right) \tag{1.17a}$$

$$\begin{aligned} \Delta z = z_{k+1} - z_k &= R_H \tan(\lambda) \cdot \theta \\ &= R_H \tan(\lambda) \sin\left(\sin(\phi_{k+1}) \sqrt{1 - \sin(\phi_k)^2} - \sin(\phi_k) \sqrt{1 - \sin(\phi_{k+1})^2} \right)^{-1} \end{aligned} \tag{1.17b}$$

$$\Delta \sin(\phi) = \cos(\theta_k) - \cos(\theta_{k+1}) = \frac{\Delta x}{R_H}, \tag{1.17c}$$

where Δx represents the propagated distance in x direction and R_H represents the radius of the helical path. The physical properties of $\tan\lambda$ and q/p_T are assumed to be constant during the propagation since energy loss of the traversing particle is omitted. Instead of

R_H, the curvature $C = 1/R_H$ is used since the corresponding uncertainties are assumed to follow a Gaussian distribution. The curvature of the helix can be calculated from the state vector variable q/p_T by

$$C = \frac{1}{R_H} = \left(\frac{q}{p_T}\right) \cdot \kappa B_z. \tag{1.18}$$

B_z represents the homogenous magnetic field of the ALICE detector in z direction in Tesla and κ is a proportionality factor. As described in Equation (1.4) the transport matrix of the helix needs to be calculated which is given by Equation (1.5). By using the Equations (1.17a) to (1.17c) the entries of the transportation matrix can be determined. The results for the entries of the transport matrix were taken from [20]. Because of correspondence with the algorithm where matrix indices start at zero by default, the indices in this work will also start with zero for the first element. The non-zero entries of the transport matrix are given by:

$$(\mathbf{F}_k)_{i,i} = \frac{\partial (f_k)_i}{\partial (s_{k-1})_i} = 1 \tag{1.19a}$$

$$(\mathbf{F}_k)_{0,2} = \frac{\partial y_{k+1}}{\partial \sin(\phi_k)} = \frac{\Delta x}{r_1^3} \tag{1.19b}$$

$$(\mathbf{F}_k)_{0,4} = \frac{\partial y_{k+1}}{\partial (q/p_T)} = \frac{(\Delta x)^2}{2 \cdot r_1^3} \cdot \kappa B_z \tag{1.19c}$$

$$(\mathbf{F}_k)_{1,2} = \frac{\partial z_{k+1}}{\partial \sin(\phi_k)} = \frac{\Delta x \cdot \tan(\lambda) \cdot \sin(\phi_k)}{r_1^3} \tag{1.19d}$$

$$(\mathbf{F}_k)_{1,3} = \frac{\partial z_{k+1}}{\partial \tan(\lambda_k)} = \frac{\Delta x}{r_1} \tag{1.19e}$$

$$(\mathbf{F}_k)_{1,4} = \frac{\partial z_{k+1}}{\partial (q/p_T)} = \frac{(\Delta x)^2 \cdot \tan(\lambda) \cdot \sin(\phi_k)}{2 \cdot r_1^3} \cdot \kappa B_z \tag{1.19f}$$

$$(\mathbf{F}_k)_{2,4} = \frac{\partial \sin(\phi_k)}{\partial (q/p_T)} = \Delta x \cdot \kappa B_z \tag{1.19g}$$

$$\text{with } r_1 = \sqrt{1 - \sin(\phi_k)^2}. \tag{1.19h}$$

The default class used to describe particle tracks is the *AliHelix* class [21] of AliROOT. Thus the calculated paths are transformed into the *AliHelix* class to further analyze the found tracks (see Appendix 5). The implementation of the Kalman filter is published on GitHub [22] and publicly available.

2 Two Dimensional Monte Carlo Simulation

A suitable test environment in form of a 2D Monte Carlo (MC) simulation was developed before the Kalman filter was implemented for real data. For that the data analysis environment *ROOT* [23] was used and the simulation consists of only one stack of detector modules. To simplify the simulation further the trapezoidal shape of the stack was not taken into account, i.e. the simulated detector has a rectangular shape. An example picture of this simulation can be seen in Fig. 2.1.
The blue rectangles represent the detector, the green tracklets represent random noise tracklets and all red tracklets together form the simulated particle track. The simulated detector uses a local coordinate system with its center at the lower left corner, the y–axis along the bottom of the detector plane and the x–axis orthogonal to the y–axis with the positive x-axis in the direction of the layers further away from the primary vertex. This coordinate system is equivalent to the one later used for real data. The noise tracklets are created with a random number generator (RNG) already included in *ROOT* with which the position, the layer and the direction of the tracklets are determined. The total number of tracklets and the maximal angle of which each tracklet can deviate from the x–axis can be adjusted. For the purpose to adjust the variable parameters faster a graphical user interface (GUI) was written which can be seen in Fig. 2.2. To set the total number of noise tracklets the variable *lines_nbr* and to change the maximum angle the variable *max_deg* can be modified. The RNG takes a seed which is used to calculate the output number so that the same initial seed creates the same output series of numbers which then translates to the same event being created. This random seed gets set with the variable *rand_seed* which increases after every event so that a new event gets produced every time but this also allows a specific event to be recreated and reevaluated.

The particle track itself gets created by randomly choosing a first hit point within the first layer of the detector and randomly picking the transverse momentum of the particle within a given range. The range can be adjusted with the parameters *min_p* and *max_p* in units of GeV/c. With the momentum the radius of the helix the particle would follow can be calculated by

$$r = \left(\frac{p_T}{B \cdot q} \right), \tag{2.1}$$

with p_T the transverse momentum of the particle in GeV/c, B the magnetic field in Tesla and q the charge in units of elementary charge e. The particle charge q gets set by the variable *part_charge*. Then the helical path, starting from the primary vertex, which is always set at the ideal interaction point, and going through the first detector layer, is calculated and the positions of the interaction points with the outer layers as well as their direction is calculated. Lastly random uncertainties to the position and the direction are

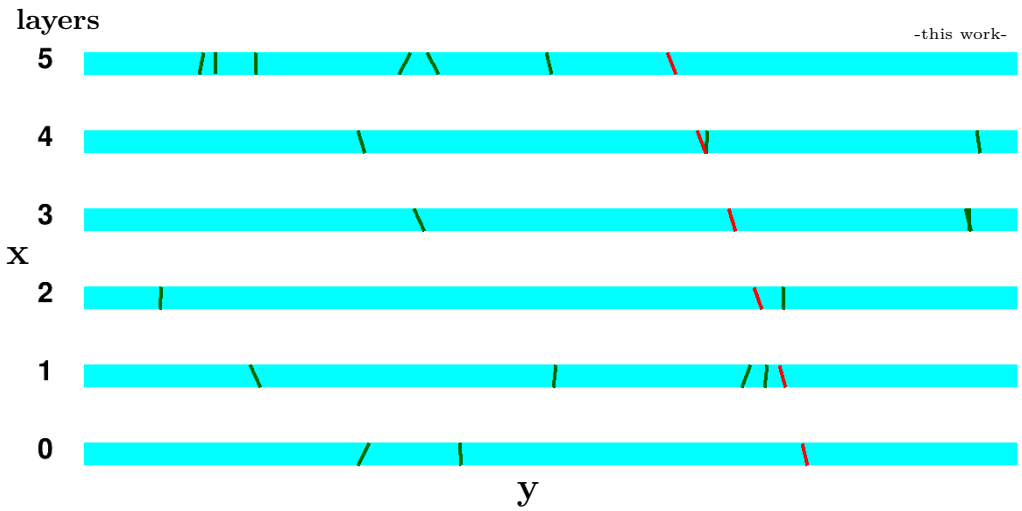

Figure 2.1: Single event of the ROOT/C++ Monte Carlo Simulation. The blue rectangles represent the different detector layers, the green tracklets the noise and the red tracklets the particle track.

added to simulate tracking and calibration uncertainties. The range of the uncertainties can be defined by the variable *max_track_pos* for the location uncertainty in mm and *max_track_deg* for the uncertainty on the angle of the direction in degrees. The detector inefficiency defines the probability that a tracklet does not get detected which can be set with the variable *layer_ineff*. Additionally the position of the last tracklet has to be within the borders of the detector to get approved as a valid track, otherwise a new track is generated.

2.1 Simple Tracking Algorithm

With the Monte Carlo Simulation in place a simple tracking algorithm was implemented which then later found its use as part of the seeding for the Kalman filter. The tracking starts at the innermost layer moving outwards where a comparison of offset and direction between the last found tracklet and each tracklet in the upper layers is done to find the next fitting tracklet. To propagate from one layer to the next, a linear estimation with direction of the last is made. The new position can be calculated by

$$\vec{x_2} = \vec{x_1} + \vec{v_1} \cdot \frac{x_2 - x_1}{|v_{x1}|}, \tag{2.2}$$

where $\vec{v_i}$ represents the direction vector, $\vec{x_i}$ represents the offset vector and x_i represents the x coordinate of tracklet i. If the tracklets are within a certain range of location, defined with the parameter *loc_unc* as percentile of the detector length (0.015 correspond to 1.5 % of the detector length), and within a certain range of the direction angle, defined with the

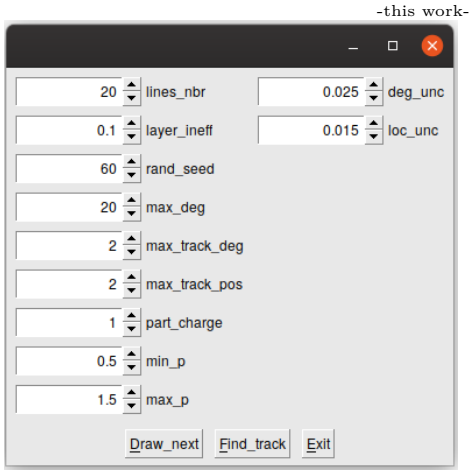

Figure 2.2: GUI of the Monte Carlo Simulation using ROOT. *Draw_next* creates a new simulation using the left parameters, *Find_track* starts a simple tracking algorithm for the current event using the right parameters. *Exit* closes the simulation.

parameter *deg_unc* as percentile of the half circle (0.025 correspond to 2.5 % of 180°), the new tracklet gets assigned to the track and set as last found tracklet and so on. The result of this algorithm for one event is depicted in Fig. 2.3. The tracklets defined as a track by the algorithm are connected with a purple line.

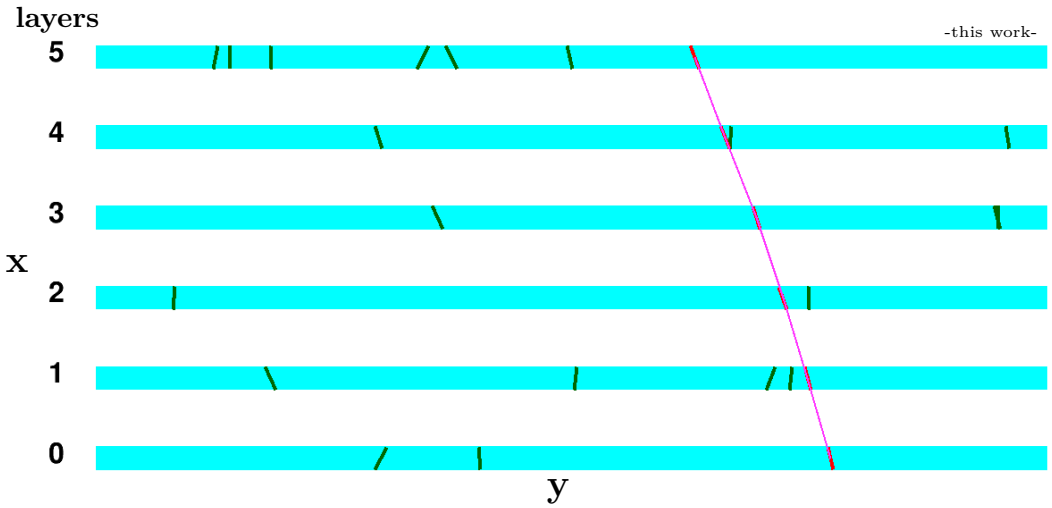

Figure 2.3: Single event of the ROOT/C++ Monte Carlo simulation after tracking. The blue rectangles represent the different detector layers, the green tracklets the noise and the red tracklets the particle track. The purple line shows which tracklets the algorithm considers as a track.

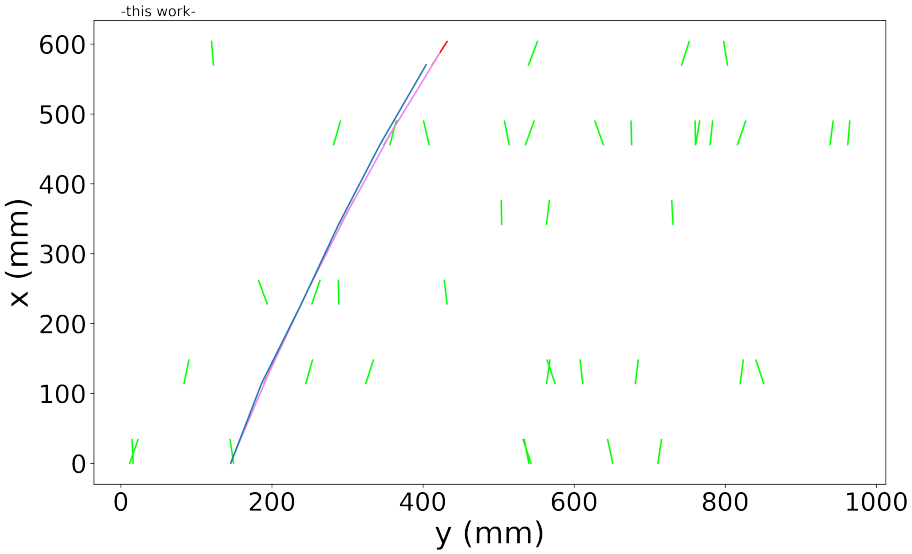

Figure 2.4: Single event of the Python Monte Carlo simulation after tracking. The green tracklets represent the noise and the red tracklets the true particle track. Which tracklets are part of the track is indicated by the purple line below the blue line which connects all tracklets corresponing to the found track. The overlapping blue line depicts the propagated y positions of the track at each x position.

2.2 Kalman filter implementation for simulated Events

A Kalman filter tracking approach in 2D for Monte Carlo data was implemented in addition to the simple tracking as discussed above. For this the simulation and simple tracking algorithm was rewritten in the programming language Python. The use of a GUI and the graphical representation of the detector were left out. The rewriting of the code was part of a rapid prototyping process which also allowed for interconnectivity to similar ongoing projects [24] since they were also developed in Python. An example representation for the simulation is shown in Fig. 2.4.

The first Kalman approach was still in two dimensions and also using a straight line instead of a helix as track model. Because of the linear model, the state vector s only has two entries:

$$s = (y, \tan\phi)^T, \tag{2.3}$$

and the propagation function is also fairly simple:

$$\Delta y = \tan\phi \cdot \Delta x, \tag{2.4}$$

$$\Delta \tan\phi = 0, \tag{2.5}$$

and the entries of the transport matrix are:

$$(\mathbf{F}_k)_{i,i} = \frac{\partial (f_k)_i}{\partial (s_{k-1})_i} \qquad = 1, \tag{2.6}$$

$$(\mathbf{F}_k)_{0,1} = \frac{\partial y_{k+1}}{\partial \tan(\phi_k)} \qquad = \Delta x, \tag{2.7}$$

$$(\mathbf{F}_k)_{1,0} = \frac{\partial \tan(\phi_{k+1})}{\partial y_k} = 0. \tag{2.8}$$

$$\tag{2.9}$$

Contrary to the Kalman filter implemented on real data, the Kalman filter on the MC data starts at the innermost layer and propagates outward and the seeding for the MC Kalman filter is only done in the first two layers of the simulated TRD. After the propagation the algorithm will search for fitting tracklets at each layer in which no tracklet is assigned to the track. For the selection of new tracklets the uncertainties on the individual state variables are used which are acquired by taking the square root of the diagonal elements from the covariance matrix. If the new tracklet exceeds a factor three of the uncertainties it is not selected for the track. If more than one tracklet fulfills this requirement, all tracklets will be investigated further as separate tracks to keep the opportunity of tracking particles which split up inside the TRD. Particle tracks which split up within the TRD come from i.e. photon conversions within or in front of the TRD where the inner layers have only one tracklet for the electon and positron path and in the outer layers the two paths are detected as seperate tracks.
In addition to the Kalman filter with the linear model, a Kalman filter with a helical track model was implemented which was then compared to the linear model. The two dimensional helical track model consists of a three dimensional state vektor

$$s = (y, \sin\phi, q/p_T)^T, \tag{2.10}$$

the propagation function used consists of the Equations (1.17a) and (1.17c) with the transport matrix entries consisting of the Equations (1.19a) to (1.19c) and (1.19g). The criteria for the tracklet selection are equal to the linear model. Both Kalman filters use the same seeding algorithm which is the algorithm described in section 2.1 with the only difference, that the seeding algorithm only operates in the first two layers. The used uncertainty ranges for the seeding algorithm can be seen in Table 2.1. The efficiency and the purity of both Kalman filters (linear and helical track model) were determined using the MC simulation and compared. For the efficiency only the found track with the most matches to the simulated true track is considered and the efficiency is calculated by dividing the number of matched tracklets by the total number of tracklets which are part of the MC track. For the purity the number of found correct tracks is divided by the

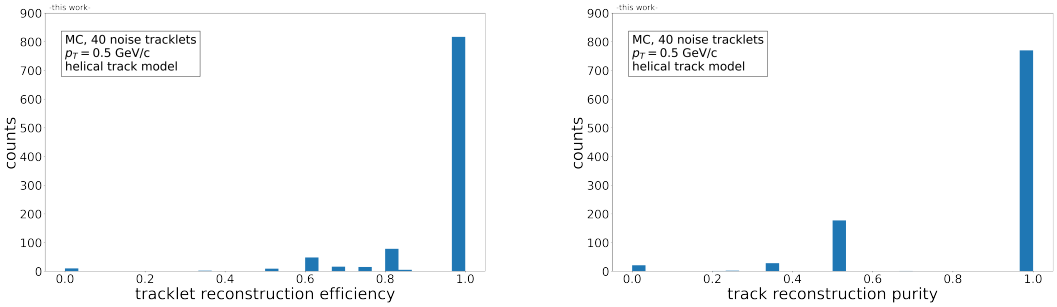

(a) Track reconstruction efficiency.

(b) Track reconstruction purity.

Figure 2.5: Efficiency (a) and purity (b) for the MC simulation. The measurements were done for 1000 events with a helical model and simulated tracks with $p_T = 0.5\,\mathrm{GeV}/c$
.

number of total found tracks. A correct track is defined by correctly finding at least half of the tracklets which are in the MC track. The condition for a correct track was set in this way because a sufficient tracking can be achieved even without finding every tracklet of the track. Those two values are calculated for 1000 different events per value of p_T and are shown in Fig. 2.5 for the helical tracking model and a track transverse momentum of $0.5\,\mathrm{GeV}/c$. The parameters used for the simulation are listed in Table 2.1. The number of noise tracklets seems to be realistic for p–Pb data and the used uncertainties seem to be underestimated compared to the tracks of p–Pb data. As shown in the histograms, in over 75 % of the cases the algorithm has a perfect efficiency and purity even for particle momenta as low as $0.5\,\mathrm{GeV}/c$. For more than 80 % of the MC tracks every tracklet corresponding to the track was found and in over 75 % of the events the MC track is also the only track that was found. In 19 % of the cases one noise track was found. The accuracy and purity increases for higher p_T values. To demonstrate this and to compare the two track models the mean of those histograms were taken for different values of p_T and plotted in Fig. 2.6.

It can be seen that the efficiency and purity for high p_T tracks are very similar for both track models. For high p_T the track curvature is close to zero so a linear estimation is reasonable but for low p_T the curvature increases so a linear estimation does not represent the particle track sufficiently well. This can be seen in figure 2.6 when looking at the values for low p_T. While the efficiency and purity for the Kalman filter with the linear track model is decreasing rapidly, both values stay constant for the Kalman filter with the helical track model until a p_T value of around $0.5\,\mathrm{GeV}/c$. The efficiency of the helical Kalman track model is close to one for whole p_T $>0.5\,\mathrm{GeV}/c$ but the purity saturates at a value of around 0.85. The reason is that with 40 noise tracklets there is a reasonable chance that for three or more noise tracklets to align well enough to get detected as a track.

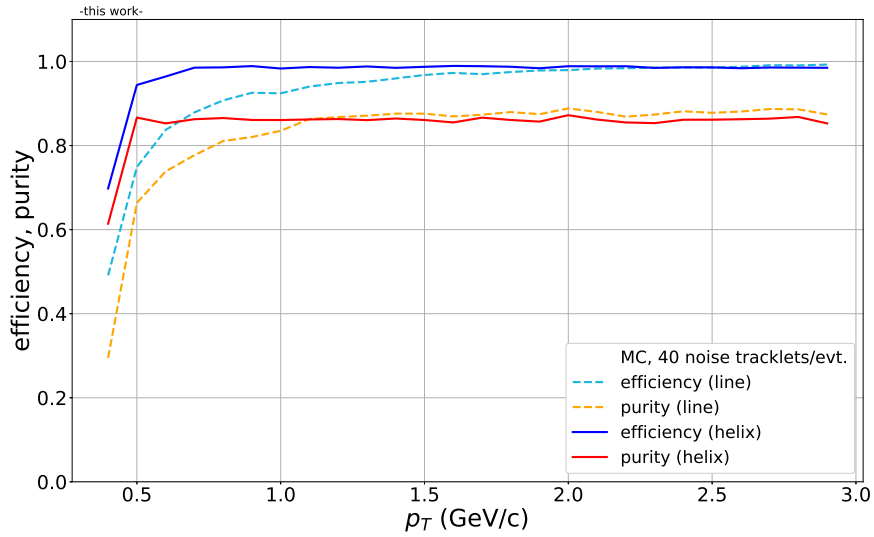

Figure 2.6: Efficiencies and purities for the helical and the linear track model in dependance of the transverse momentum for 40 noise tracklets per event.

The measurements were retaken for 120 and 200 noise tracklets (see Appendix 5). The measurements showed that the purity decreases significantly for both track models due to the increased possibility of randomly aligned tracklets and the eficiency for the helical track model decreases as well. For lower p_T tracks the efficiency and purity for the helical track model is still better than for the linear track model. As a result this measurement shows that the helical model is superior for the reconstruction of particle tracks at a lower p_T, so only the Kalman filter with the helical track model will be developed further to be used for real ALICE TRD data.

Variable	Value
lines_nbr	40
max_deg	20°
max_track_pos	2 mm
max_track_deg	2°
part_charge	−1
layer_ineff	10 %
loc_unc	3°
deg_unc	2.5°

Table 2.1: Variables for the MC simulation and the simple tracking algorithm. The variables are explained in chapter 2.

3 Kalman filter Tracking

3.1 Kalman filter implementation for real data

After the successful test with the MC simulation in two dimensions, the simulation was expanded to three dimensions, the track model was adjusted corresponding to Equations (1.17a) to (1.17c) and the transport matrix was updated in accordance to Equations (1.19a) to (1.19g). This simulation proved that the algorithm is working, so the Kalman filter could be applied to the real data. The real data consists of around 700.000 events from proton–lead collisions with an energy of 5.02 TeV per nucleon pair which were recorded with the ALICE detector in 2016. One example event is shown in a 3D display in Fig. 3.1. Depicted in blue are the propagated TPC tracks and the different chambers of the TRD are in different colours indicating their functionality. Turquoise chambers are fully operational, red chambers were turned off and the other colours indicate exactly what part of the chamber was not working, e.g. low drift high voltage. The functionality of the detector chambers are not taken into account during the Kalman filter algorithm. For the tracklets (depicted in white and yellow) a new calibration scheme was applied which was never used before and which made the direction measurement of the tracklets more precise. The new calibration is described in chapter 1.1.3.1. A few key features of the tracking algorithm were reworked during the process of implementing it on the real data. In contrary to the MC Kalman filter which searches its tracklets from the innermost layer going outwards, the Kalman filter implemented on the real data goes from the outer layers inwards. This has the advantage that tracks of particles which split up inside the TRD can be better reconstructed and also the occupancy of primary and secondary tracks is lower in the outer layers. Now each time a new tracklet needs to be selected as the next part of the new track, only one possible tracklet is chosen which creates the need for a more extensive selection algorithm which has to reliably select the best fitting tracklet in accordance to the uncertainties of the current state and the measurement. For this reason a χ^2 criterion for the selection of new measurements was implement according to the Equation (1.6). To get selected as a new measurement for the track the new tracklet has to have the lowest predicted χ^2 value of all tracklets and this value also has to be below a certain threshold. The speed of the algorithm was measured with the use of the build in c++ time library *<chono>*. For 2000 p–Pb events a computation time of 19.95 s were required on a laptop with 16 GB RAM and an Intel®Core^{TM} i7 processor with 8 cores and a clock frequency of 1.8 GHz.
In addition a matching between the tracklets found by the Kalman filter and TRD tracklets which were matched with TPC tracks is made to be able to determine which Kalman track corresponds to which TPC track. For this matching each tracklet of the event gets assigned an index number to unambiguously identify each tracklet and during the matching process each TPC track is compared with each track found by the Kalman filter. The Kalman

track with the most matching tracklets is then the one which finally is matched with the TPC track. In Fig. 3.2a the propagated helical paths of matched TPC and Kalman tracks are depicted. With less than 70 cm of fitting range numerous propagated Kalman tracks overlap with the TPC tracks all the way to the primary vertex which is about 3 m away from the TRD but some of the propagated tracks diverge significantly from the TPC tracks. Reasons for that are that some of the Kalman tracks might not have a tracklet in every layer of the TRD because of some turned off detector chambers. Additionally the calibration of the tracklets is brand new and was done for only two of the used 13 runs for the measurements. For completeness the Kalman tracking was done for the same events but also including the primary vertex as an additional constrain of the track and as depicted in Fig. 3.2b all Kalman tracks are now nearly perfectly fitting the TPC tracks.

3.2 Reconstruction efficiency

With the TPC tracks that are matched with Kalman filter tracks, the Kalman filter reconstruction efficiency can be calculated. For that only TPC tracks are used which have at least four matched TRD tracklets because the Kalman filter only considers tracks with at least four tracklets. Over half of the tracklets corresponding to the TPC track need to be part of the Kalman filter track which is matched with the TPC track to be considered as successfully reconstructed. Every TPC track with at least four tracklets without a matched Kalman filter track or a matched Kalman filter track which has less or equal than 50 % in common with the TPC track is counted as not reconstructed. The result of the efficiency measurements can be seen in Fig. 3.3.
For comparison the track reconstruction efficiency of the Kalman filter implemented for the Monte Carlo simulation is also plotted. The efficiency of the real data has a peak at a p_T value of around 2 GeV/c with an efficiency value of around 0.9. The reconstruction efficiency decreases rapidly for $p_T < 1\,\mathrm{GeV}/c$. This might be related to the fact, that tracks with a higher curvature have a higher possibility of passing through multiple supermodules of the TRD and the currently implemented Kalman filter is not able to search through multiple sectors. This circumstance will be changed in the near future. Another reason for the drop in efficiency might be because the current seeding algorithm propagates in a linear manner so tracks with a high curvature have a higher possibility to not get selected. The reconstruction efficiency decreases linearly for $p_T > 2\,\mathrm{GeV}/c$ from an efficiency of 0.9 for 2 GeV/c to an efficiency value close to 0.8 for a p_T value of 10 GeV/c. The reason for that is currently unknown and requires further studies.
The efficiency for the real data follows a similar trend as the one for the MC simulation but the efficiency value for the MC simulation is higher than the one for the real data

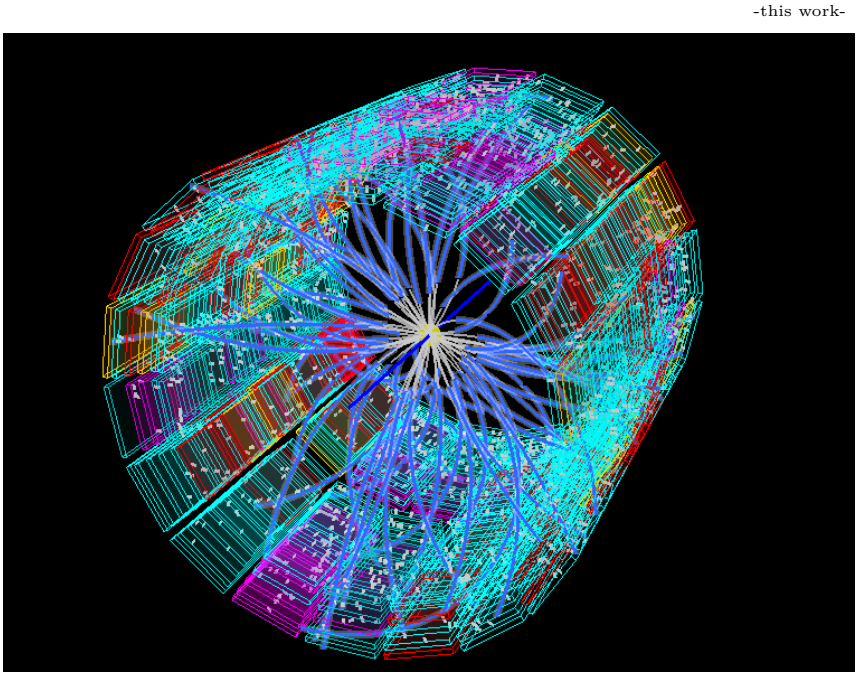

Figure 3.1: 3D view of one example p–Pb event. The TPC tracks are depicted in blue and the TRD tracklets in white and yellow, where the yellow tracklets are associated to a Kalman track. The colours of the TRD chambers mark different grades of functionality where turquoise chambers are fully operational and red ones turned off.

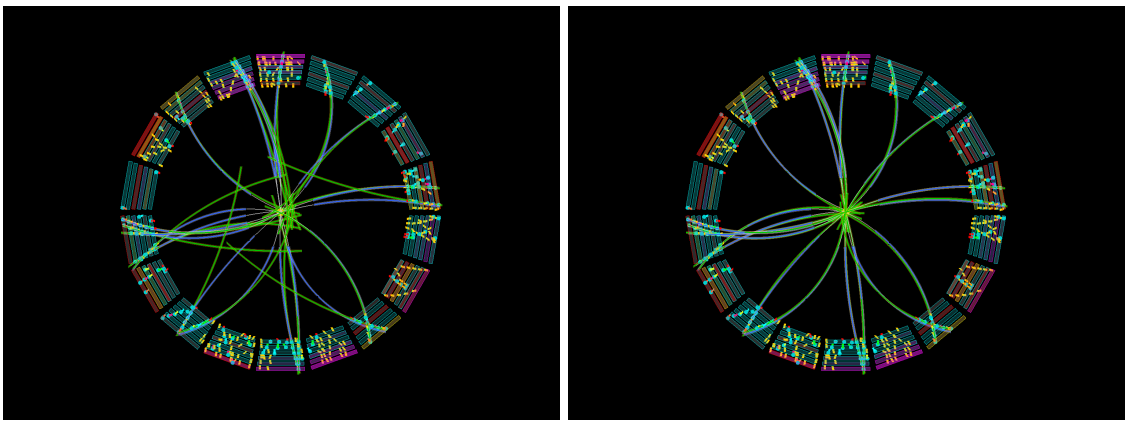

(a) (b)

Figure 3.2: 2D view of the same event as in 3.1 with matched Kalman and TPC tracks. The TPC tracks are depicted in blue and the Kalman tracks in green. On the left the Kalman tracks are propagated without and on the right with the primary vertex used as additional measurement during the Kalman filter algorithm.

with an average value of around 0.96. The reasons for the difference in the efficiencies can be accounted to the uncertainties of the tracklets in the MC simulation being most likely underestimated, the measurement in the MC simulation being made in 2D, which results in two less parameters that have to fit and the fact that the calibration of the events was only done for two runs but applied to all 13 events so there might be some inconsistencies in the calibration. Also whether a layer is working or not is defined randomly in the MC simulation so the possibility of two subsequent layers missing is low compared to the real data which results in a lower efficiency for the Kalman filter on real data. The efficiency measurements were used to determine the values for the χ^2 threshold and the uncertainties on the measured tracklets which are needed for the measurement matrix. This was done by iteratively adjusting the parameters on efficiency measurements made for a few example events. The measurement matrix which was used in the Kalman filter consists of the squared uncertainties on the corresponding measured variables (y, z, $\sin\phi$, $\tan\lambda$) which are written in the diagonal elements. The used values of the different parameters are shown in Table 3.1.

3.3 Transverse momentum resolution of the Kalman filter

To determine the TRD stand alone Kalman filter transverse momentum resolution, correlation plots between the q/p_T measured by the TPC and the q/p_T determined by the Kalman filter were made for the Kalman tracks which were matched with the TPC tracks. These correlation plots were made for the tracking with and without the constraint to the primary vertex and are depicted in Fig. 3.4. The left plot shows the correlation between the TPC and the Kalman q/p_T without the use of the primary vertex. The tracks are separated by positive and negative particle charge and the different colours are a measure of the number of tracks in a certain area. The plot shows a decreased width of the distribution for higher q/p_T (which correlates to smaller p_T) and a broader distribution for low q/p_T. Most particles in the TRD have surpassed their minimum ionizing particle point when they reach a momentum below $0.5\,\mathrm{GeV}/c$ so the energy loss per traveled distance is increased. The increased energy loss results in a strong decrease of transverse momentum relative to the original transverse momentum. This might be the reason for the asymmetry at high q/p_T on the left side of Fig. 3.4, where the q/p_T from the Kalman filter is systematically higher than the TPC q/p_T. Numerous Kalman tracks can be seen to have the opposite charge of the TPC tracks. Reasons for the wrongly assigned particle charge are outliers in the measured tracklets of the tracks and missing measurements in some layers of the TRD which results in a helix of opposite charge to be fitted. On the right side of Fig. 3.4 the correlation plot with the use of the primary vertex is depicted. The plot shows a strong correlation for the whole range of TPC momenta and only few tracks

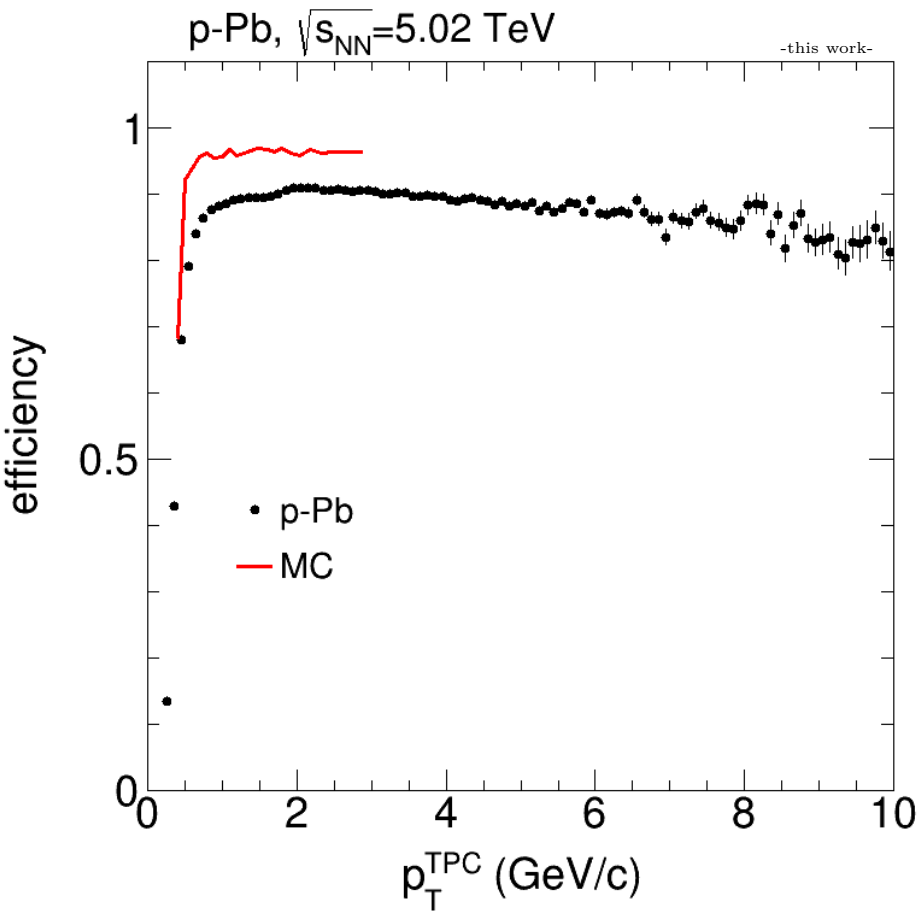

Figure 3.3: Track reconstruction efficiency for TPC matched tracks to Kalman filter tracks (black). The uncertainties of the measurements show the standard deviation from the mean. For comparison the track reconstruction efficiency of the Kalman filter implemented for the Monte Carlo simulation is plotted in red.

with an opposite charge. As expected, the correlation increases significantly by including the primary vertex. To determine the p_T resolution, projections of the 2D plots to the Kalman filter q/p_T axis are performed for each TPC q/p_T bin. A Gaussian function is fitted to the projected histograms of the Kalman filter q/p_T values. A selection of these plots is depicted in Fig. 3.5. The Gaussian fits are made twice to increase the fit to the data. The standard deviation σ, the mean μ and the maximum of the histograms in Fig. 3.5 are calculated and used as start parameters for the first Gaussian fit. The first fit is performed in a range of two standard deviations around the mean. The resulting values of the amplitude, μ and σ from the first fit are used as the starting parameters for the second fit and the fit is done for a range of 1.2σ around the mean.

From the Gaussian fits the standard deviation is taken and divided by the q/p_T value taken

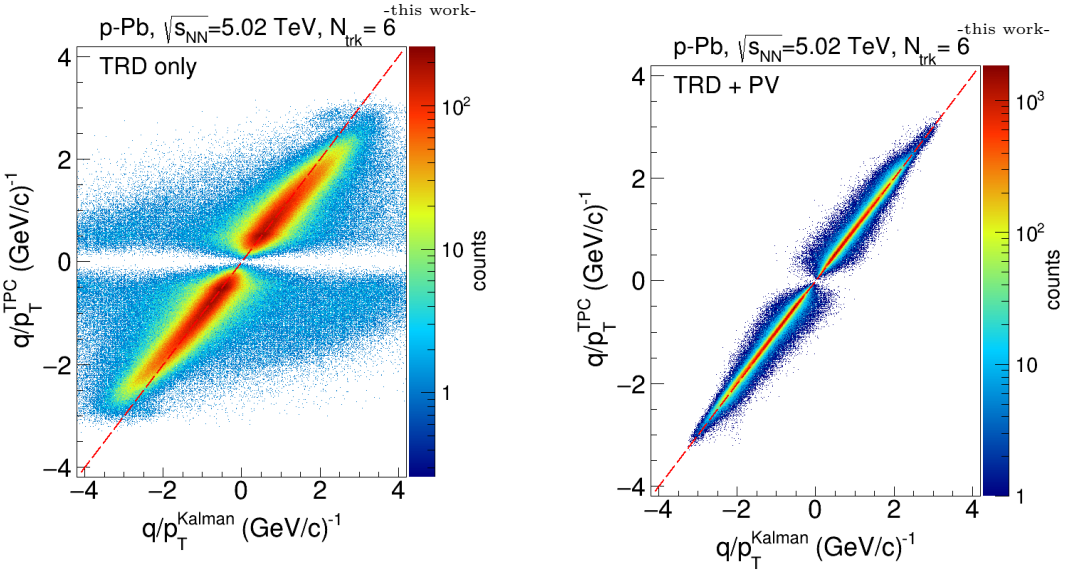

Figure 3.4: Correlation plots between TPC and Kalman q/p_T without (left) and with (right) the use of the primary vertex (PV).

from the TPC to obtain the q/p_T resolution for the Kalman filter. The transverse momentum resolution in percent is depicted as a function of the TPC transverse momentum measurement in Fig. 3.6.

The figure shows that for high q/p_T tracks with six tracklets (corresponding to low p_T) and the use of the primary vertex a resolution of below 2.5 % is achieved which goes up to 8 to 9 % for lower q/p_T. Without the use of the primary vertex a resolution of 10 to 11 % is achieved for the high q/p_T tracks which goes up to over 30 % for low q/p_T. The q/p_T resolution is not symmetrical. Positively–charged particles overall have a worse p_T resolution than negatively–charged particles and the reasons for this are currently unknown and require further studies. The q/p_T resolution measurements were used to determine the uncertainties on the fifth variable of the state vector q/p_T. This was done by iteratively adjusting the uncertainty and reviewing the impact on the resolution. The uncertainties on the state vector are used for the initial estimate of the covariance matrix where the squared uncertainties are written on the diagonal elements of the matrix. The initial value of the q/p_T has a great impact on how significant the influence of a new measurement is on the value of q/p_T during the correction. For the uncertainties of the other state variables, the uncertainties on the measured tracklets were used. The used values of the different parameters are shown in Table 3.1.
Additionally $q \cdot p_T$ correlation plots were made and the corresponding p_T resolution with and without the primary vertex constraint were calculated. The different plots can be

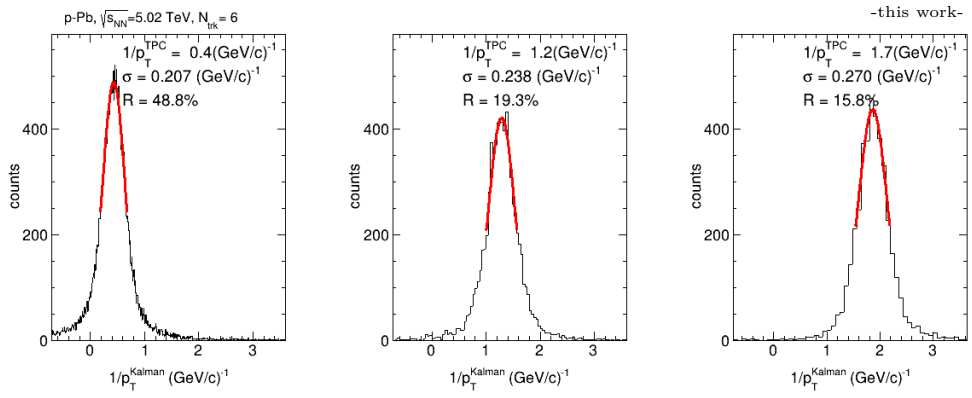

Figure 3.5: Kalman filter p_T distributions for different TPC p_T with a Gaussian fit. The bin width is $0.005\,\mathrm{GeV}/c$. R represents the calculated p_T resolution.

Parameter	Value
χ^2 threshold	18.5
y uncertainty	0.45 cm
z uncertainty	2 cm
$\sin\phi$ uncertainty	$\sin 7°$
$\tan\lambda$ uncertainty	$\sin 18°$
q/p_T uncertainty	$18\,c/\mathrm{GV}$

Table 3.1: Initial parameters of the Kalman filter for real data.

seen in the Appendix 5. Contrary to the q/p_T resolution, the p_T resolution does not follow a Gaussian distribution.

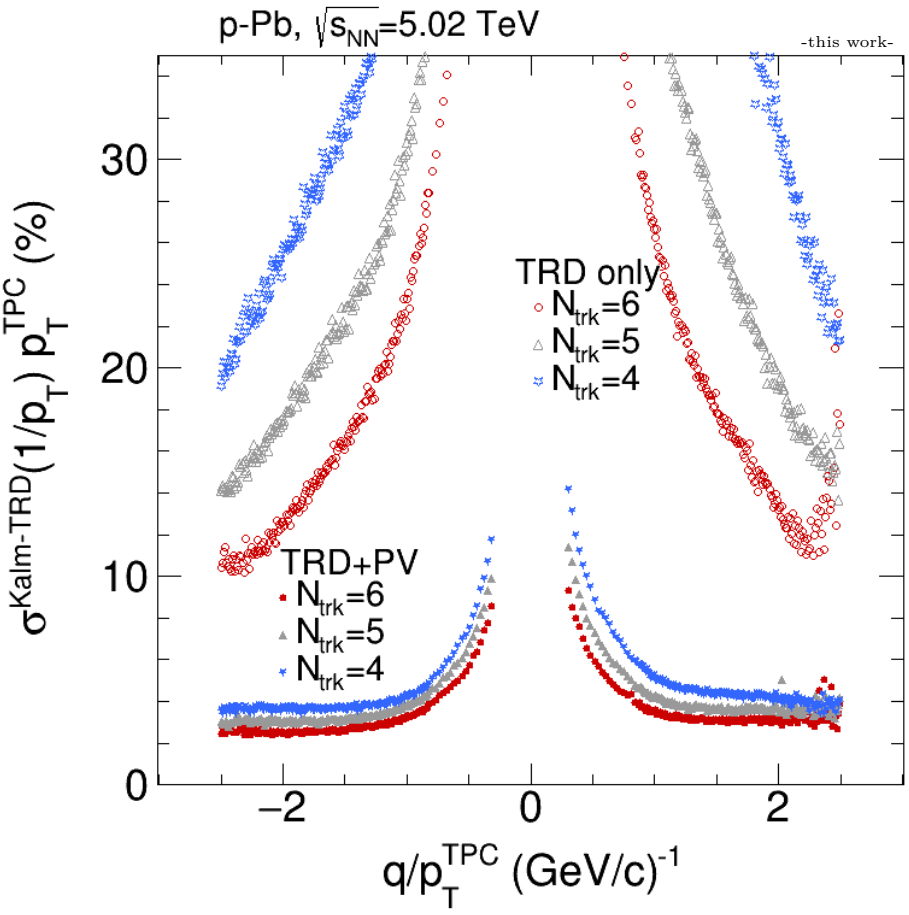

Figure 3.6: TRD momentum resolution as a function of the matched TPC q/p_T. Red markers correspond to 6, grey ones to 5 and blue ones to 4 tracklets per track. The measurements where only the TRD was used are depicted by hollow markers and full markers are used for resolutions which were acquired by using the TRD and the primary vertex constraint.

4 Reconstruction of Photon Conversions and Nuclear Interactions

The implemented Kalman filters functionality has been confirmed so it can be used to perform some physics analyses. At first the Kalman filter was used to search for photon conversions happening in or close in front of the TRD. For that a secondary vertex finder was implemented which is using the calculated helical particle paths from the Kalman filter to search for intersections or close encounters of these paths. The goal of the secondary vertex finder is to find the point of closest approach between two helices. The algorithm works by numerically minimizing the distance between two points on these two helices which is time consuming. To improve the performance of the algorithm two additional steps before the numerical optimization were implemented. A two dimensional analytical calculation of intersection points and an analytical estimate of the closest points of these two helices in three dimensions. Only when the estimated points are less than 15 cm away from each other, then those estimates are used to calculate the numerical points with closest distance to each other. Two helices are considered to share a common secondary vertex if the distance of closest approach is below 5 cm. Within the scope of this work the 2D calculation of circular interaction points/closest point was implemented as well as a function for calculating the path of the helix at a given radius, which will be described further. For the 2D calculation the radii of both circles r_1 and r_2 as well as their center positions in a 2D plane x_1, x_2, y_1, y_2 are used to calculate either the interaction points if both circles overlap or the point halfway in between both circles if they do not overlap. The calculations for the 2D interaction points are done in a local coordinate system in which both circle centers are on the local x-axis. Then the following equations are valid at the interaction points:

$$x_{loc}^2 + y_{loc}^2 = r_1^2 \tag{4.1}$$

$$(d - x_{loc}^2) + y_{loc}^2 = r_2^2 \tag{4.2}$$

$$\text{with } d = \sqrt{(x_1 - x_2)^2 + (y_1 - y_2)^2} \tag{4.3}$$

the distance between the circle centers.

x_{loc} and y_{loc} describe the coordinates of the interaction points in the local coordinate system. Now the values of x_{loc} and y_{loc} can be calculated:

$$x_{loc} = \frac{d^2 - r^2{}_2 + r_1^2}{2d} \tag{4.4}$$

$$y_{loc1/2} = \pm\sqrt{r_1^2 - x_{loc}^2} \tag{4.5}$$

with y_{loc1}being the positive and y_{loc2} the negative solution.

and in the global coordinate system the intersection points are given by

$$x_{glob1/2} = x_1 + x_{loc} \cdot \frac{x_2 - x_1}{d} - y_{loc1/2} \cdot \frac{y_2 - y_1}{d} \tag{4.6}$$

$$y_{glob1/2} = y_1 + x_{loc} \cdot \frac{y_2 - y_1}{d} + y_{loc1/2} \cdot \frac{x_2 - x_1}{d} \tag{4.7}$$

$$\text{with } d = \sqrt{(x_1 - x_2)^2 + (y_1 - y_2)^2} \tag{4.8}$$

the distance between the circle centers.

The closest point between the two circles is calculated as

$$x_{glob} = x_1 + \left(r_1 + \frac{d - (r_1 + r_2)}{2} \right) \cdot \frac{x_2 - x_1}{d} \tag{4.9}$$

$$y_{glob} = y_1 + \left(r_1 + \frac{d - (r_1 + r_2)}{2} \right) \cdot \frac{y_2 - y_1}{d}. \tag{4.10}$$

After the closest points between the two circles are calculated, the paths of the helices at the radii of these closest points in relation to the center is calculated analytically. The performed calculations were taken from [25] where the function is described in detail. The path is then used to calculate an estimate on the closest points on the helices and only if those are close enough (15 cm) the real closest points are numerically calculated and then it gets decided whether or not a secondary vertex is present. A secondary vertex is present if the numerically calculated distance of closest approach is below 5 cm. The calculated secondary vertices can then be used to identify and examine several particle interactions.

4.1 Photon Conversions

Photons can convert into an $e^+ + e^-$ pair once they come into the vicinity of a nucleus. Due to the zero mass of the photon the decay opening angle in the lab frame is close to zero, so both particles are emitted parallel to each other. The particle tracks seperate from each other due to the applied magnetic field. To identify photon conversions from secondary vertices several selection criteria on Armenteros-Podolanski variables [26] were applied. An Armenteros-Podolanski (AP) plot is used to identify decayed particles in dependance of the resulting particle momenta without exactly knowing the daughter PIDs. The original particles direction $\overrightarrow{q}$ is calculated by adding the momentum vectors $\overrightarrow{p}^i$ of the resulting particles at the position of the secondary vertex and normalizing the resulting vector. On the y–axis of the AP plot the transverse momentum of the decay products q_T in relation to the momentum of the original particle is plotted against the longitudinal momentum

asymmetry α which is calculated by

$$\alpha = \frac{q_L^+ - q_L^-}{q_L^+ + q_L^-}, \tag{4.11}$$

where q_L^+ represents the longitudinal momentum of the positively-charged decay product and q_L^- represents the longitudinal momentum of the negatively-charged decay product. The longitudinal momentum is calculated by

$$q_L^i = \overrightarrow{q} \cdot \overrightarrow{p}^i, \tag{4.12}$$

and the transverse momentum q_T is calculated by

$$q_T = \sqrt{(q_L^i)^2 \cdot |\overrightarrow{p}^i|^2}. \tag{4.13}$$

The transverse momentum relative to the original particle is the same for the resulting electron and positron:

$$q_T = q_T^+ = q_T^-. \tag{4.14}$$

From the two values q_T and α of a decaying particle and therefore its position on the AP plot the type of the particle is determined. Based on the AP variables, several selection criteria are applied to identify candidates of photon conversions. For two found tracks with a shared secondary vertex to be identified as photon conversion candidates, the transverse momentum in the labratory system p_T of each of the tracks has to be between 40 and 500 MeV/c and the tracks need to have opposite charge. The transverse momentum in the center of mass system q_T of the incoming photon has to be between 0 and 20 MeV/c and the longitudinal momentum asymmetry α has to be between a value of -0.2 and 0.2. Additionally no TPC track can be present within 10 cm of the secondary vertex and the direction of the photon has to point to the primary vertex. For this the scalar product of the normalized direction vector of the photon and the normalized offset vector of the secondary vertex has to be above a value of 0.9.
Additional selection criteria are applied which only allowed certain constellations of shared and independent tracklets between the two reconstructed Kalman tracks. These selection criteria are made in a way that they require a certain number of tracklets in certain layers which are unique for each track and a number of tracklets in certain layers which are shared among both tracks. The cuts are listed in Table 4.1. The first cut for example specifies that both tracks have to have at least two shared tracklets in the first three layers and at least two independent tracklets in the last three layers. An example of such a photon conversion candidate can be seen in Fig. 4.1a. Pictures of photon candidates which are used in other cuts can be seen in Fig. 4.1. In Fig. 4.1b a photon conversion can be seen which satisfies

Cut No.	No. shared	Layers	No. indep.	Layers
1	$\geqslant 2$	0,1,2	$\geqslant 2$	3,4,5
2	$\geqslant 3$	0,1,2,3	$\geqslant 1$	3,4,5
3	$\geqslant 1$	0,1,2	$\geqslant 3$	2,3,4,5
4	$\geqslant 1$	0,1	$\geqslant 3$	1,2,3,4,5
5	$= 0$	0,1,2	$\geqslant 4$	0,1,2,3,4,5

Table 4.1: Table of used selection criteria for the plot of radial distances of secondary vertices for photon conversion candidates (see Fig. 4.2). The table shows the number of required tracklets with a certain label (shared or independent) and the layers in which those requirements have to be fulfilled.

cut 5 where no shared tracklets are present and the secondary vertex is found in front of the TRD. In Fig. 4.1c a photon conversion is depicted with one shared tracklet in the first layer which fulfills cut number 3 and 4 and in Fig. 4.1d there are two individual photon conversions with the right one fulfilling cut 2 and the left one fulfilling cut 1. The position and direction of the two photon conversions indicates that they possibly originate from a shared secondary vertex and therefore from a possible π^0 decay. The radii of the secondary vertices (depicted as red points in Fig. 4.1) which are found are plotted in a histogram depicting the radial distribution of the secondary vertices. This histogram is shown in Fig. 4.2. It shows only photon candidates which fulfill the previously mentioned cuts and are depicted by which cut they pass. The distribution shows that the most secondary vertices are found between the different layers instead of the center of these layers and that almost all recorded secondary vertices are found in front of layer 3. The most secondary vertices are found between the second and third layer. The distributions of the cuts 1,3 and 4 have peaks between the first and second layer as well as between the second and third layer of the TRD and almost no found secondary vertices after the third layer. Of these three cuts, cut 1 has the most found photon candidates. Cut 2 has an additional peak between the third and fourth layer because the cut searches for shared tracklets up to the fourth layer. Cut 5 is responsible for almost all of the found photon conversion candidates with secondary vertices below a radius of 280 cm where the conversion happens so far in front of the TRD that no tracklets are shared by both reconstructed tracks. Further studies are required to identify wheter the observed peaks between the different layers of the TRD have a physical background or rather are artifacts from the secondary vertex finder algorithm.

For the photon conversion candidates the uncorrected p_T distribution is depicted in Fig. 4.3. The $\frac{1}{slope}$ value of the exponential fit lies in the magnitude of around 140 MeV. The plot also demonstrates that the Kalman filter is able to find photon conversion candidates for p_T as low as $0.2\,\mathrm{GeV}/c$.

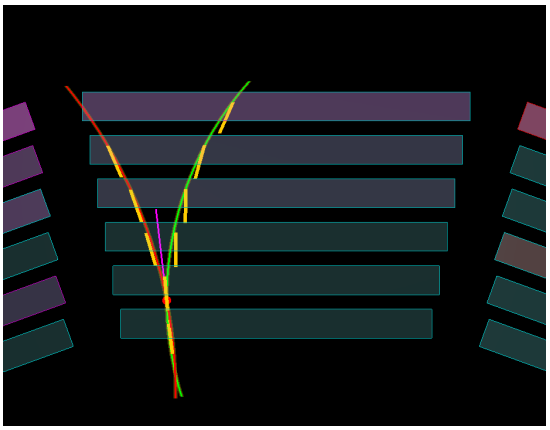

(a) The candidate has 2 shared tracklets in the first two layers and 3 or 4 independent tracklets in the upper 4 layers. This candidate fulfills the cuts 1,3 and 4 (see Table 4.1).

-this work-

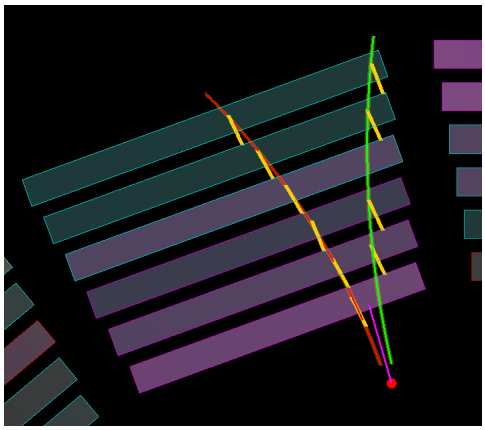

(b) The candidate has no shared tracklets in any layers but 6 or 4 independent tracklets and a shared secondary vertex. This candidate fulfills cut 5 (see Table 4.1).

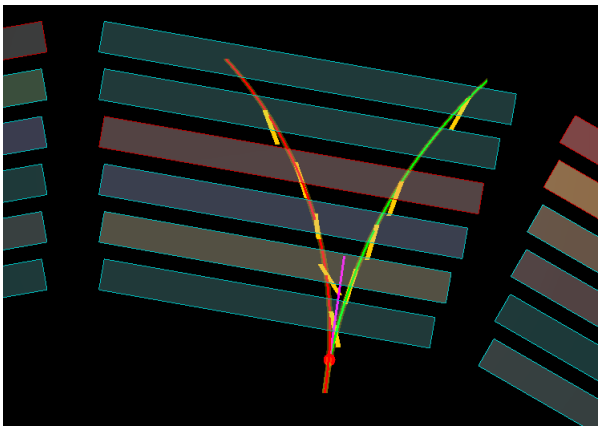

(c) The candidate has 1 shared tracklet in the first layer and 4 independent tracklets in the upper 5 layers. This candidate fulfills cuts 3 and 4 (see Table 4.1).

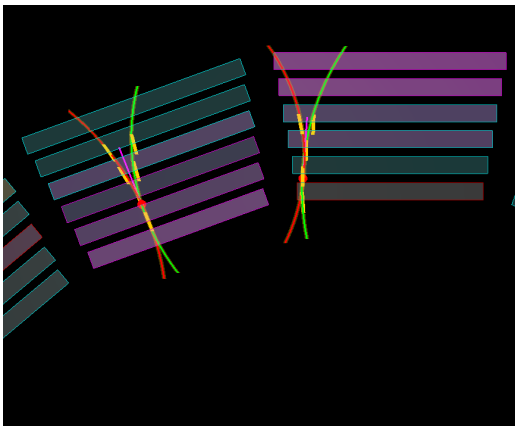

(d) Two candidates were found which might have a shared secondary vertex. The left candidate fulfills cut 1 and the right candidate fulfills cut 2 (see Table 4.1).

Figure 4.1: Pictures of photon candidates seen in the XY-plane. Tracklets are depicted in yellow. The calculated particle tracks are shown in red (for positively–charged particles) or green (for negatively–charged particles). The secondary vertex is depicted as a red dot and the purple line depicts the direction of the incoming photon.

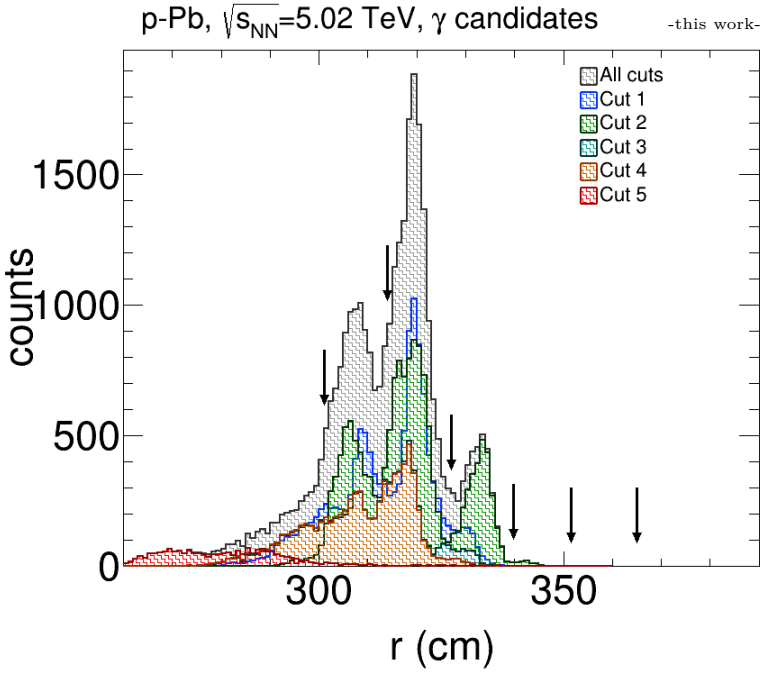

Figure 4.2: Radial distribution of secondary vertices for photon conversion candidates. On each photon candidate which is selected via criteria of an AP plot additional selection criterias are applied and the results are shown in this histogram. The selection criteria are described in Table 4.1. The black arrows show the mean radius of the readout pads of each layer.

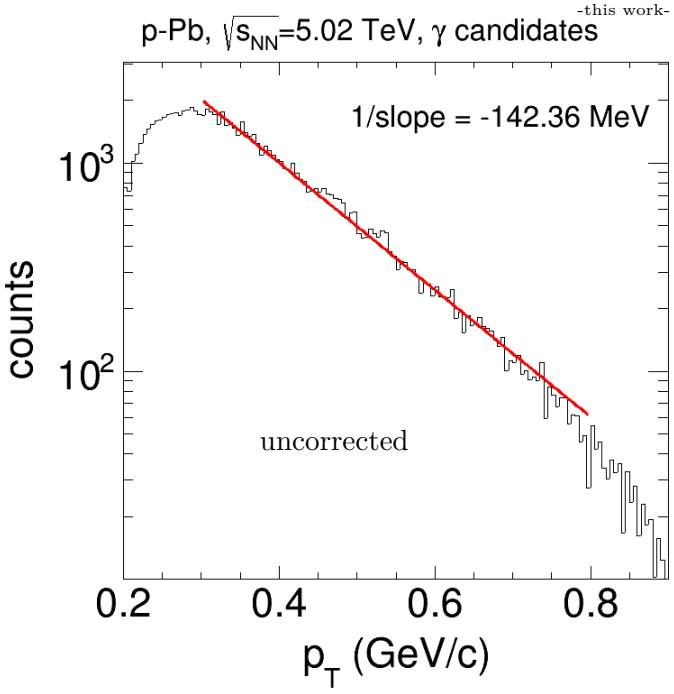

Figure 4.3: Uncorrected p_T distribution for photon conversion candidates with exponential fit.

4.2 Nuclear Interactions

Nuclear interactions take place, when incoming particles interact with nuclei within the TRD and produce a shower of multiple other particles. The expected nuclear interactions consist of an incoming particle track reconstructed by the TPC which produces a shower of new particles within the TRD. The reconstructed multiple particle tracks should share a secondary vertex with the incoming particle track. The secondary vertex finder was used to find candidates for nuclear interactions which happen inside the TRD. For that the nuclear interactions had to fulfill two criteria: First at least three individual tracks need to contribute to the found secondary vertex and second the found secondary vertex had to be within 3 cm of a TPC track. A selection of found nuclear interactions can be seen in Fig. 4.4. In Fig. 4.4a a simple nuclear interaction candidate is depicted where three participating Kalman tracks were found. In Fig. 4.4b two nuclear interaction candidates were found where one interaction is decaying outward of the detector and one interaction is decaying inwards. The inward decay might be caused by one decay product of the outward decay. In Fig. 4.4c and 4.4d two nuclear interaction candidates are depicted with multiple contributing tracks and a cascade like shower. As well as for the photon candidates in Fig. 4.2 the radial distribution of the secondary vertices is plotted for the nuclear candidates and is depicted in Fig. 4.5. The radial distribution of the nuclear interaction points is depicted as a function of the number of tracks which contribute to the secondary vertex. The course of the distributions are similar for the different numbers of allowed tracks. All distributions have peaks at the centers of the first, second and third layer of the TRD with the second layer having the most interactions, followed by the first layer and then the third layer. A fourth peak can be seen between the first and second layer of the TRD. A possible reason for the peaks at the center of the detection chambers might be the large radiation length of the readout pads ($X/X_0 = 0.77\,\%$ [27]) and the electronics right behind them ($X/X_0 = 1.18\,\%$ [27]) but further studies are required. The information about independent and shared tracklets is gathered and a selection criterion was made which forced at least four independent tracklets in each of the upper three layers. This selection criterion did not change the course of the radial distributions but significantly decreased the number of found nuclear interaction candidates. The effect of different selection criteria applied to the nuclear interactions will require further studies. Additionally the $\frac{\partial E}{\partial x}$ distribution of the TPC tracks which were matched with the nuclear candidates found in the TRD is plotted in Fig. 4.6. The results show that most of the recorded nuclear interactions are caused by pions.

-this work-

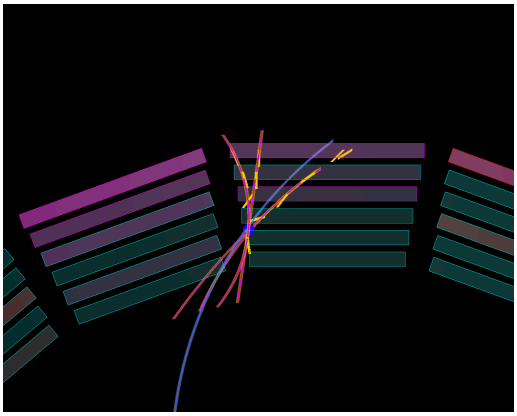

(a) Nuclear interaction candidate with three contributing tracks.

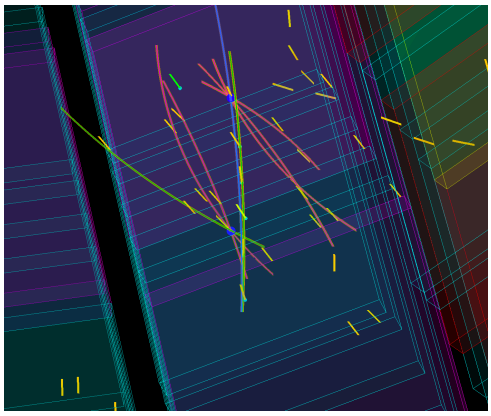

(b) Two nuclear interaction candidates. The right nuclear candidates decays outward while the other is decaying inwards to the detector.

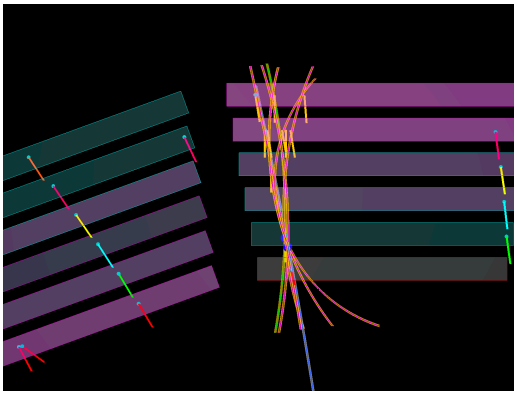

(c) Nuclear interaction candidate with a cascade-like shower.

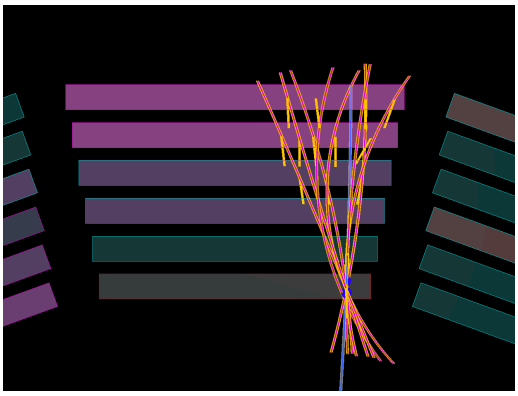

(d) Nuclear interaction candidate with a cascade-like shower.

Figure 4.4: Pictures of nuclear interaction candidates. Tracklets are depicted in yellow. The incoming TPC track is shown in blue. The nuclear interaction point is depicted as a blue dot and the red and green lines depict the different tracks contributing to the interaction. The green line was used to identify the first found track of the interaction.

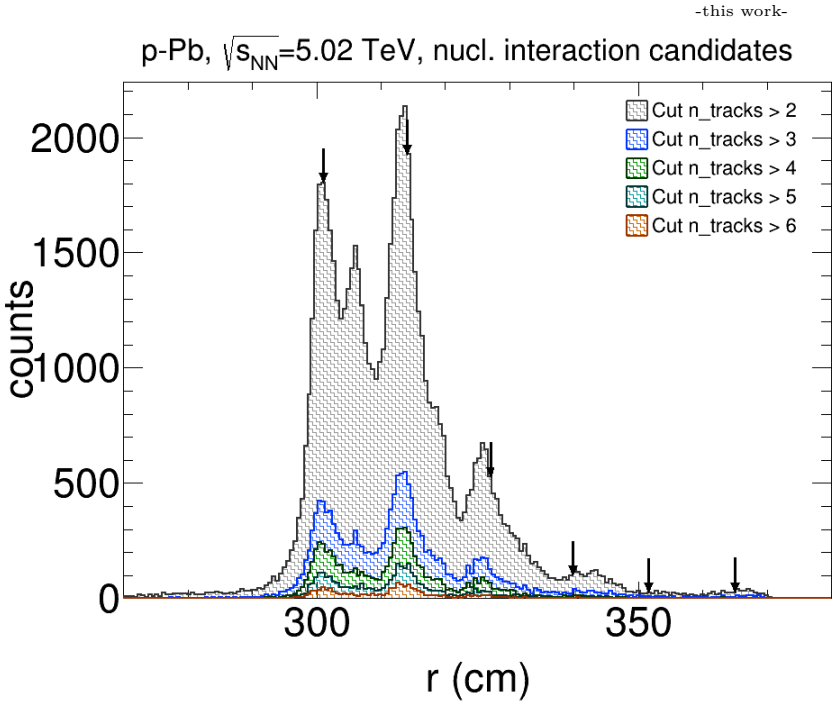

Figure 4.5: Radial distribution of secondary vertices of nuclear interaction candidates. The radial distribution is plotted as a function of the number of contributing tracks. The black arrows indicate the mean radius of the readout pads of each layer.

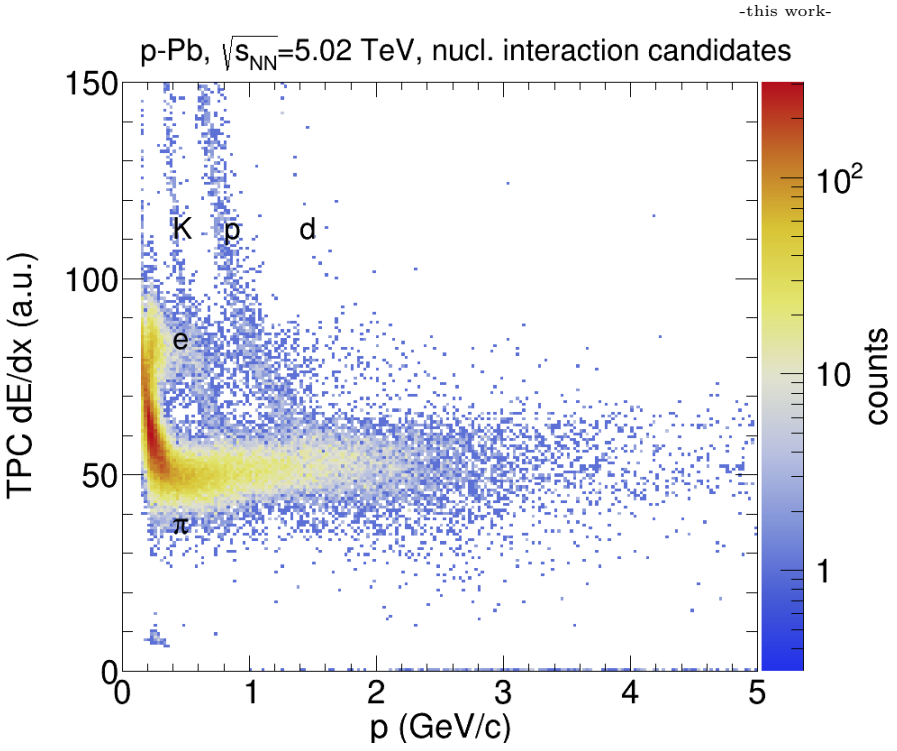

Figure 4.6: $\frac{\partial E}{\partial x}$ distribution of TPC tracks matched with nuclear interaction candidates found in the TRD.

5 Conclusion and Outlook

During this bachelor thesis a Kalman filter tracking algorithm was implemented for the Transition Radiation Detector in ALICE. To test the algorithm a 2D Monte Carlo simulation with a simple tracking algorithm, a Kalman filter tracking algorithm with linear track model, and a Kalman filter tracking algorithm with a helical track model was developed. The purity and efficiency of the Kalman filter was determined. It showed that the helical track model has a higher tracking purity and efficiency, especially for particles with $p_T < 1\,\mathrm{GeV}/c$. For the 3D simulation a Kalman filter with a helical track model was implemented for the proof of concept. For data from p–Pb collisions at $\sqrt{s_{NN}} = 5.02\,\mathrm{TeV}$ a Kalman filter with a helical track model was implemented. The efficiency of reconstructing to TPC tracks matched tracks was determined to be between 0.8 and 0.9 for transverse momenta between $0.5\,\mathrm{GeV}/c$ and $10\,\mathrm{GeV}/c$. In addition the p_T resolution was determined with and without a primary vertex constraint for Kalman filter tracks matched to TPC tracks. The q/p_T resolution with the use of a primary vertex is between 2.5 % for high q/p_T tracks and 9 % for low q/p_T. Without the use of the primary vertex the q/p_T resolution for 6 tracklets is around 9 % for high and over 30 % for low q/p_T.
A pre-existing secondary vertex finder was optimized and used to reconstruct candidates for nuclear interactions and photon conversions in front of or within the TRD. The found photon candidates were selected by selection criteria based on Armenteros-Podolanski variables and further topological selection criteria. Close to 190000 photon conversions were identified out of around 700000 p–Pb events. The calculated radial distribution of secondary vertices showed that most of the secondary vertices were between the different active TRD layers. For the nuclear interaction candidates, cuts were made on the number of found tracks contributing to the nuclear interaction. During the analysis around 69000 nuclear interactions with a matched corresponding TPC track were identified. The radial distribution of nuclear interaction points showed that the nuclear interactions happen within the TRD layers where the readout pads are placed and a made $\frac{\partial E}{\partial x}$ plot demonstrated that most found nuclear interactions originate from pions. As a result of this bachelor thesis a working tracking algorithm based on a Kalman filter approach was developed, implemented and shown to be a reliable tool with a high efficiency and purity for identifying nuclear interactions and photon conversions in front of and within the TRD.

In the future additional improvements to the implemented Kalman filter could be applied. Those include the implementation of an additional fit to the found tracks to increase the p_T resolution, the introduction of χ^2 cut to the found tracks based on the number of tracklets to improve the purity of the Kalman filter and reworking of the algorithm to search for particle tracks in multiple sectors and stacks of the TRD. In addition to that measurement uncertainties based on the multiplicity of the detector could be implemented and the seeding algorithm improved. The speed of the algorithm could be increased and

additionally reworked so that the secondary vertex finder and the photon conversion / nuclear interaction criteria could allow for more conversions/ interactions to be identified with a higher efficiency and purity. These improvements along with the repairs of the TRD for Run 3 and an improved calibration of the TRD data based on the TRD stand alone tracking developed during this thesis can significantly improve the functionality of the Kalman filter.

Appendix

Calculations for the Alihelix class

The result of the Kalman filter for an individual track is the state vector

$$s = (y, z, \sin\phi, \tan\lambda, q/p_T)^T, \tag{5.1}$$

at the propagation variable x. The Alihelix class needs eight parameters to fully describe the helix and the state vector needs to be transformed into these parameters. To aquire these parameters, the offset and momentum vector of the particle is first calculated and then rotated into the global coordinate system. The offset vector in the local coordinate system is given by the propagation variable of the Kalman filter (x), the first (y) and the second (z) variable of the state vector. The momentum vector is calculated by assuming the charge of the particle to be either $1\,e$ or $-1\,e$, so the transverse momentum and charge are given by:

$$p_T = \frac{1}{|(q/p_T)|}, \tag{5.2}$$

$$q = (q/p_T) \cdot p_T. \tag{5.3}$$

The momentum vector is then given by:

$$p_x = p_T \cdot \sqrt{1 - \sin(\phi)^2}, \tag{5.4}$$

$$p_y = p_T \cdot \sin(\phi), \tag{5.5}$$

$$p_z = p_T \cdot \tan\lambda. \tag{5.6}$$

The offset and momentum vector are then rotated into the global coordinate system (X,Y,Z) and the curvature C is calculated with Equation (1.18). Then the individual

variables of the *AliHelix* are given by:

$$AliHelix[0] = Y + \frac{1}{C} \cdot \frac{p_X}{p_T}, \tag{5.7}$$

$$AliHelix[1] = Z, \tag{5.8}$$

$$AliHelix[2] = \arcsin\left(\frac{p_X}{p_T}\right), \tag{5.9}$$

$$AliHelix[3] = \frac{p_Z}{p_T}, \tag{5.10}$$

$$AliHelix[4] = C, \tag{5.11}$$

$$AliHelix[5] = X - \frac{1}{C} \cdot \frac{p_Y}{p_T}, \tag{5.12}$$

$$AliHelix[6] = p_T, \tag{5.13}$$

$$AliHelix[7] = p_Z. \tag{5.14}$$

$$\tag{5.15}$$

The parameters in the AliHelix format are then used to further analyze the found particle tracks.

Efficiency and purity of the Kalman filters in the Monte Carlo simulation

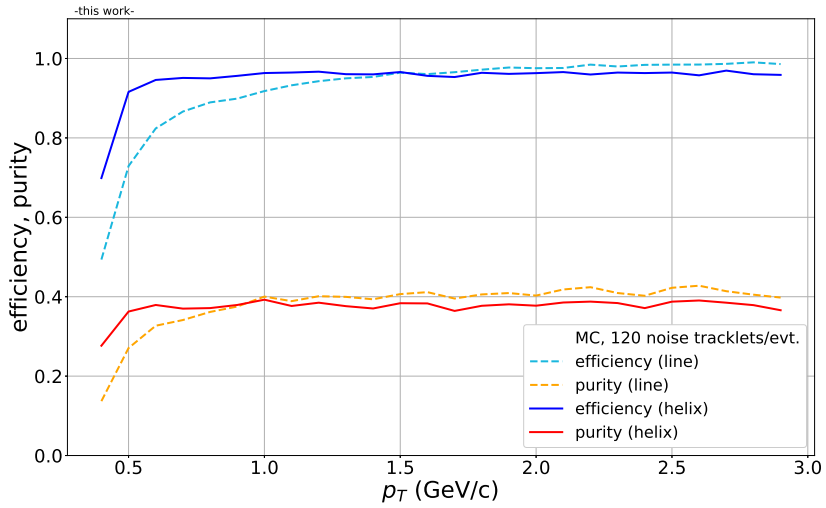

Figure 5.1: Efficiencies and purities for the helical and the linear track model in dependance of the transverse momentum for 120 noise tracklets per event.

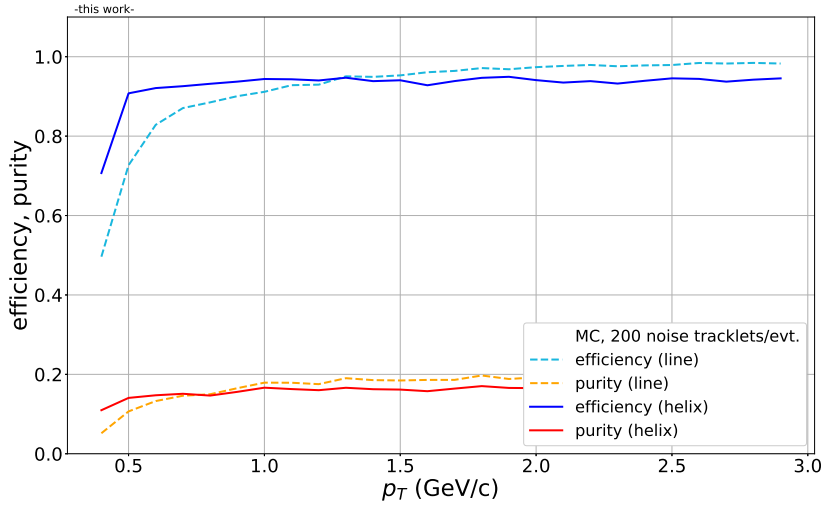

Figure 5.2: Efficiencies and purities for the helical and the linear track model in dependance of the transverse momentum for 200 noise tracklets per event.

p_T resolution of the Kalman Filter

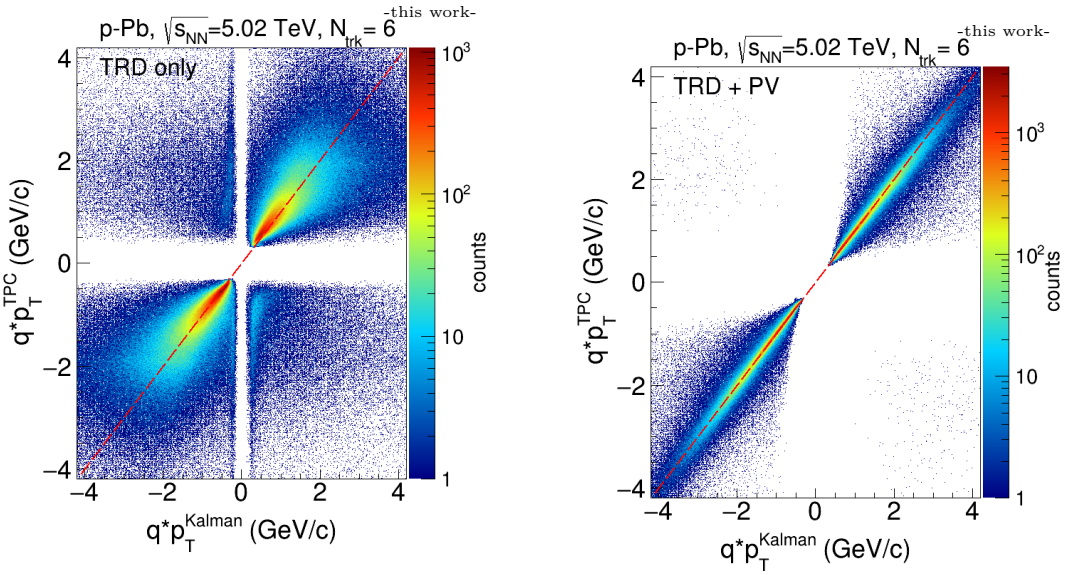

Figure 5.3: Correlation plots between TPC and Kalman p_T without (left) and with (right) the use of the primary vertex (PV).

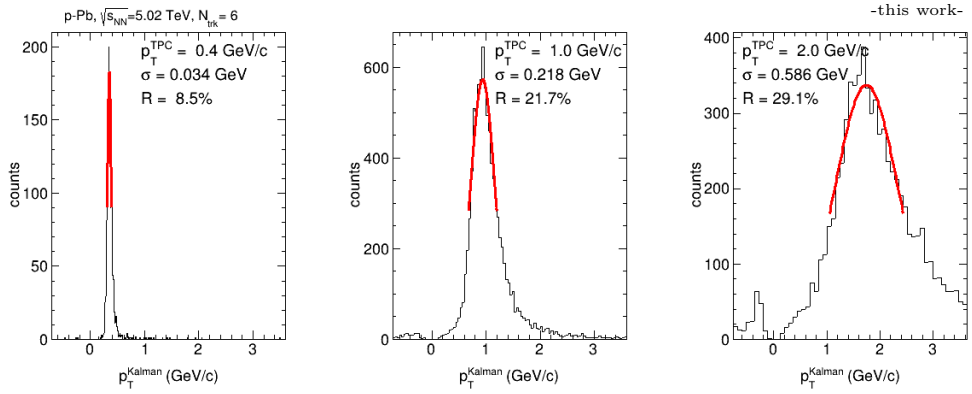

Figure 5.4: Kalman filter p_T distributions for different TPC p_T with a Gaussian fit. The bin width is $0.005\,\mathrm{GeV}/c$. R represents the calculated p_T resolution.

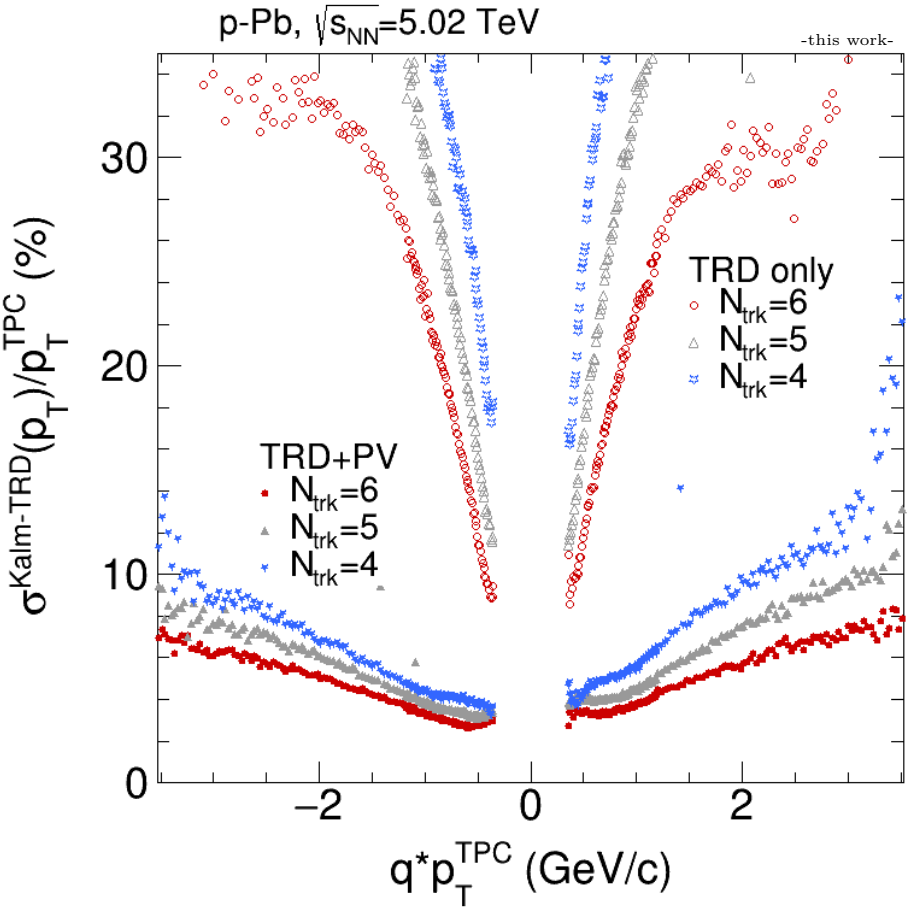

Figure 5.5: TRD momentum resolution as a function of the matched TPC p_T. Red markers correspond to 6, grey ones to 5 and blue ones to 4 tracklets per track. The measurements where only the TRD was used are depicted by hollow markers and full markers are used for resolutions which were acquired by using the TRD and the primary vertex constraint.

Literature

[1] D. Boyanovsky et al. "Phase Transitions in the Early and Present Universe." In: *Annual Review of Nuclear and Particle Science* 56.1 (Nov. 2006), pp. 441–500. DOI: 10.1146/annurev.nucl.56.080805.140539. URL: http://dx.doi.org/10.1146/annurev.nucl.56.080805.140539.

[2] J.D. Bjorken. "Highly Relativistic Nucleus-Nucleus Collisions: The Central Rapidity Region." In: *Phys. Rev. D* 27 (1983), pp. 140–151. DOI: 10.1103/PhysRevD.27.140.

[3] H. Appelshauser et al. "Hadronic expansion dynamics in central Pb + Pb collisions at 158-GeV per nucleon." In: *Eur. Phys. J. C* 2 (1998), pp. 661–670. DOI: 10.1007/s100520050168.

[4] M.C. Abreu et al. "Evidence for deconfinement of quarks and gluons from the J / psi suppression pattern measured in Pb + Pb collisions at the CERN SPS." In: *Phys. Lett. B* 477 (2000), pp. 28–36. DOI: 10.1016/S0370-2693(00)00237-9.

[5] E. Andersen et al. "Strangeness enhancement at mid-rapidity in Pb Pb collisions at 158-A-GeV/c." In: *Phys. Lett. B* 449 (1999), pp. 401–406. DOI: 10.1016/S0370-2693(99)00140-9.

[6] M. M. Aggarwal et al. "Observation of Direct Photons in Central 158AGeVP208b+P208b Collisions." In: *Physical Review Letters* 85.17 (Oct. 2000), pp. 3595–3599. DOI: 10.1103/physrevlett.85.3595. URL: http://dx.doi.org/10.1103/PhysRevLett.85.3595.

[7] Lucia Leardini. " Measurement of neutral mesons and direct photons in Pb–Pb collisions at $\sqrt{s}$NN = 2.76 TeV with the ALICE experiment at the LHC." Presented 20 Nov 2017. PhD thesis. 2017. URL: https://doi.org/10.11588/heidok.00023756.

[8] Esma Mobs. "The CERN accelerator complex - 2019. Complexe des accélérateurs du CERN - 2019." In: (July 2019). General Photo. URL: https://cds.cern.ch/record/2684277.

[9] The ALICE Collaboration. "Performance of the ALICE experiment at the CERN LHC." In: *International Journal of Modern Physics A* 29.24 (Sept. 2014), p. 1430044. DOI: 10.1142/s0217751x14300440. URL: http://dx.doi.org/10.1142/S0217751X14300440.

[10] B Alessandro et al. (ALICE Collaboration). *ALICE: Physics Performance Report. ALICE physics performance : Technical Design Report*. Ed. by B Alessandro. Vol. 32. Technical Design Report ALICE. revised version submitted on 2006-05-29 15:15:40. Geneva: CERN, 2005. DOI: 10.1088/0954-3899/32/10/001. URL: https://cds.cern.ch/record/879894.

[11] K Aamodt et al. (ALICE Collaboration). "The ALICE experiment at the CERN LHC." In: *Journal of Instrumentation* 3.08 (Aug. 2008), S08002–S08002. DOI: 10.1088/1748-0221/3/08/s08002. URL: https://doi.org/10.1088%2F1748-0221%2F3%2F08%2Fs08002.

[12] B Abelev et al. (ALICE Collaboration). *Technical Design Report for the Upgrade of the ALICE Inner Tracking System*. Tech. rep. CERN-LHCC-2013-024. ALICE-TDR-017. Nov. 2013. DOI: 10.1088/0954-3899/41/8/087002. URL: https://cds.cern.ch/record/1625842.

[13] Shreyasi Acharya et al. (ALICE Collaboration). "The ALICE Transition Radiation Detector: construction, operation, and performance." In: *Nucl. Instrum. Meth. A* 881 (2018), pp. 88–127. DOI: 10.1016/j.nima.2017.09.028.

[14] Alexander Schmah. *private communication*.

[15] Jason Barrella. *private communication*.

[16] Xixiang Liu et al. "A Simplified Kalman Filter for Integrated Navigation System with Low-Dynamic Movement." In: *Mathematical Problems in Engineering* 2016 (Jan. 2016), pp. 1–9. DOI: 10.1155/2016/3528146.

[17] Mengde Zhang et al. "Comparison of Kalman Filters for Inertial Integrated Navigation." In: *Sensors* 19 (Mar. 2019), pp. 1–2. DOI: 10.3390/s19061426.

[18] Steven Lantz et al. *Speeding up Particle Track Reconstruction using a Parallel Kalman Filter Algorithm*. 2020.

[19] Rudolph Emil Kalman. "A New Approach to Linear Filtering and Prediction Problems." In: *Transactions of the ASME–Journal of Basic Engineering* 82.Series D (1960), pp. 35–45.

[20] Johannes Hendrik Stiller. "Full kinematic reconstruction of charged B mesons with the upgraded Inner Tracking System of the ALICE Experiment." Presented 11 May 2016. PhD thesis. 2016. URL: https://cds.cern.ch/record/2153601.

[21] Marian Ivanov. *Implementation of the AliHelix class*. URL: https://github.com/alisw/AliRoot/blob/master/STEER/STEER/AliHelix.cxx.

[22] Alexander Schmah. *TRD self tracking repository*. URL: https://github.com/aschmah/TRD-self-tracking.

[23] R. Brun & F. Rademakers. "ROOT: An object oriented data analysis framework." In: *Nucl. Instrum. Meth. A* 389 (1997). Ed. by M. Werlen & D. Perret-Gallix, pp. 81–86. DOI: 10.1016/S0168-9002(97)00048-X.

[24] Martin Kroesen. *private communication*.

[25] Thomas Ullrich. *Parametrization of a helix*. 1997. URL: https://www.star.bnl.gov/webdata/dox/html/StHelix_8cc_source.html.

[26] Christian Lippmann. "Particle identification." In: *Nucl. Instrum. Methods Phys. Res., A* 666.arXiv:1101.3276 (Jan. 2011). 61 pages, 30 figures, 148–172. 61 p. DOI: 10.1016/j.nima.2011.03.009. URL: http://cds.cern.ch/record/1323010.

[27] In: *Nuclear Instruments and Methods in Physics Research Section A: Accelerators, Spectrometers, Detectors and Associated Equipment* 881 (Feb. 2018), pp. 88–127. DOI: 10.1016/j.nima.2017.09.028. URL: http://dx.doi.org/10.1016/j.nima.2017.09.028.

Acknowledgement

At first I would like to thank Priv. Doz. Dr. Yvonne Pachmayer for giving me the opportunity to write my bachelor thesis working in the ALICE group and all the help I got writing my thesis as well as the constructive discussions and guidance throughout the last months.
I would also like to thank Prof. Dr. Klaus Reygers for agreeing to be the second referee for this thesis and his advice as well as constructive input for this thesis.
Thanks go to M. SC. Martin Kroesen for proofreading my thesis.
I want to thank the entire ALICE group for providing a very enjoyable work environmentand their help whenever it was needed.
Last but not least I want to thank my supervisor Dr. Alexander Schmah who always motivated me and helped me to overcome many of the hurdles of this bachelor thesis. I also want to thank him for proofreading my thesis and having an open ear for me even late in the evenings or on weekends.

Selbstständigkeitserklärung

Ich versichere, dass ich diese Arbeit selbstständig verfasst und keine anderen als die angegebenen Quellen und Hilfsmittel benutzt habe.

Heidelberg, den 7. Oktober 2020

.....

Unterschrift